Geophysical Journal International

Geophys. J. Int. (2014) **199,** 631–647
GJI Geodynamics and tectonics

doi: 10.1093/gji/ggu279

A perturbation method and its application: elastic tidal response of a laterally heterogeneous planet

Chuan Qin, Shijie Zhong and John Wahr

Department of Physics, University of Colorado at Boulder, Boulder, CO 80309*, USA. E-mail: chuan.qin@colorado.edu*

Accepted 2014 July 17. Received 2014 July 11; in original form 2014 February 21

SUMMARY

Theory has been long established for computing the elastic response of a spherically symmetric terrestrial planetary body to both body tide and surface loading forces. However, for a planet with laterally heterogeneous mantle structure, the response is usually computed using a fully numerical approach. In this paper, we develop a semi-analytic method based on perturbation theory to solve for the elastic response of a planetary body with lateral heterogeneities in its mantle. We present a derivation of the governing equations for our second-order perturbation method and use them to study the high-order tidal effects caused by mode coupling between degree-2 body tide forcing and the laterally heterogeneous elastic structure of the mantle. We test our method by applying it to the Moon in which small long-wavelength lateral heterogeneities are assumed to exist in the elastic moduli of the lunar mantle. The tidal response of the Moon is determined mode by mode, for lateral heterogeneities with different depth ranges within the mantle and different horizontal scales. Our perturbation method solutions are compared with numerical results, showing remarkable agreement between the two methods. We conclude that our perturbation method provides accurate results and can be adapted to address a variety of forward and inverse response problems.

Key words: Lunar and planetary geodesy and gravity; Dynamics of lithosphere and mantle; Planetary interiors.

1 INTRODUCTION

The interior structure and properties of terrestrial planetary bodies, including the Earth, are important for understanding planetary dynamic evolution. Seismology, by investigating elastic wave propagation in planetary interiors, is undoubtedly the most powerful method for exploring planetary interior structures. In the past two decades, seismological techniques have developed rapidly, and numerous tomographic models of the Earth's interior structure have been derived from seismological data (Dziewonski 1984; Van der Hilst *et al.* 1997). It has been demonstrated that long-wavelength lateral heterogeneities exist in the Earth's mantle, and are concentrated mainly at spherical harmonic degree 2. The dominance of degree 2 is most notable in the deep mantle, caused by two antipodal seismically slow anomalies below the central Pacific and Africa. However, seismological studies of other planetary bodies are limited to the Moon by the Apollo missions (e.g. Nakamura *et al.* 1982). Even for the Moon, due to limited seismic data, it has proved challenging to construct a tomographic model of the lunar interior.

Some knowledge of the interior structure of a planetary body may be obtained by analysing the elastic and viscoelastic response to other forces, such as tidal forces. This requires highly accurate observations of tidal deformation (often done using space geodetic methods) and efficient analytical or numerical techniques for determining the dynamic response of planetary bodies. The theoretical framework for computing the elastic response of a homogenous or spherically symmetric planetary body (i.e. a 1-D model) has long been established to help understand the dynamic response of a spherically symmetric planet to tidal forces at short timescales (Longman 1962; Longman 1963; Farrell 1972). Later, this formulation was extended to include viscoelasticity in spherically symmetric models for surface mass loading problem (e.g. Wu & Peltier 1982). However, finding a general analytic framework for computing the response of a laterally heterogeneous planetary body is still a challenge. For a planetary body with a 3-D structure consisting of small lateral heterogeneities, a perturbation theory is generally used. Tromp & Mitrovica (2000) used a perturbation method to develop a normal-mode formulation for solving the surface loading response of a viscoelastic aspherical planet. Wang (1990) applied a perturbation method to study the Earth's tidal deformation for a mantle with heterogeneities in the elastic moduli. More commonly, though, fully numerical approaches are used to solve for the response of a planetary body with 3-D structures (e.g. Kaufmann & Wu 2002; Zhong *et al.* 2003; Latychev *et al.* 2005; Latychev *et al.* 2009). One example is the finite element code CitcomSVE, which was originally developed to solve the postglacial rebound problem

© The Authors 2014. Published by Oxford University Press on behalf of The Royal Astronomical Society.

Downloaded from http://gji.oxfordjournals.org/ at University of Colorado on August 29, 2014

for a 3-D incompressible viscoelastic Earth's mantle (Zhong *et al.* 2003) and was later modified to include compressibility (A *et al.* 2013).

The main goal of this study is to develop a new perturbation method that can determine the elastic response of planetary bodies with 3-D structures. Although the method is generally applicable to different planetary bodies, we limit our analyses to the Moon's tidal response in this paper. The recent GRAIL mission aims to investigate the interior structure of the Moon by measuring the lunar gravity field with unprecedented precision (Konopliv *et al.* 2013; Lemoine *et al.* 2013; Zuber *et al.* 2013). Until future seismological investigations can be made, studies of the lunar tidal response provide a possible approach for constraining the long-wavelength structure and material properties of the lunar mantle (Zhong *et al.* 2012). The basic idea relies on the fact that the harmonic degree-2 tidal force, when applied to the Moon with laterally heterogeneous structure in the lunar mantle, will excite not only degree-2 terms, but also non-degree-2 terms, in the response.

The Moon displays a number of hemispherical asymmetries, including higher topography on the farside of the Moon (Zuber *et al.* 1994), and a concentrated distribution of both the mare basalts (Wieczorek *et al.* 2006) and deep moon quake (DMQ) events on the nearside (Nakamura 2005). A recent statistical study of the correlation between the locations of DMQ epicentres and the high-concentration mare basalt regions supports the hypothesis that the long-wavelength features of the early lunar mantle may have survived to the present day (Qin *et al.* 2012). By assuming that a harmonic degree-1 and order-1 structure can best represent such global asymmetry, Zhong *et al.* (2012) used CitcomSVE (Zhong *et al.* 2003; A *et al.* 2013) to solve for the response of the lunar mantle to degree-2 tidal forcing, and explicitly determined the amplitudes of what appeared to be the largest spherical harmonic coefficients in the solution.

In this paper, we present a new perturbation method that permits a semi-analytic solution for the elastic tidal response of a planetary body with a 3-D compressible mantle, and we apply the method to study the tidal response of a laterally varying Moon. We are motivated by the following considerations. First, we try to understand mode coupling effects between the tidal forcing and a laterally heterogeneous (i.e. 3-D) structure. Those coupling effects tend to be weak, and can be obscured by noise in numerical analyses. Secondly, we show that our perturbation method can provide an efficient, alternative method for tidal response calculations, and we use it here to present the first benchmark of a 3-D numerical model.

Our perturbation analysis can model the effects of lateral heterogeneities in a planet's solid mantle, but not in its fluid core. Because of the high mobility of a fluid, the core is likely to have much smaller lateral heterogeneities than the mantle. This, combined with the large depth of the core for most planetary bodies, implies that in most cases it is reasonable to ignore the impact of the lateral heterogeneities in the core on the tidal response.

Lateral heterogeneities in the mantle are likely to exist both in the density and in the elastic moduli, that is the first Lamé parameter and the shear modulus. To avoid mathematical complications, we do not include lateral heterogeneities in the density or the Lamé parameter in this paper, but focus our analysis on the effects of lateral heterogeneities only in the shear modulus. Lateral heterogeneities in density and the Lamé parameter will be incorporated into our formulation in a further study.

The paper is organized as follows. In Section 2, we derive the governing equations of our second-order perturbation method. In Section 3, we describe the matrix forms of the governing equations, illustrate the mode coupling process, and derive a propagator matrix solution method. In Section 4, we apply our perturbation method to a laterally heterogeneous Moon and do forward calculations of the high-order tidal response for a variety of laterally heterogeneous structures. We also compare our perturbation results with the numerical results (i.e. benchmarks). In the last section, we summarize our results and discuss some potential future applications of our perturbation method.

2 GOVERNING EQUATIONS AND PERTURBATION THEORY

2.1 Governing equations

We start from the governing equations for the tidal response of an elastic, compressible, and spherically symmetric planet. In this paper, we define the entire mantle and crustal materials overlying the fluid core as the solid 'mantle', and restrict the solution region to the mantle. The equation of motion in the mantle (Farrell 1972; Wahr *et al.* 2009) is

$$\nabla \cdot \vec{\vec{\tau}} - \rho_0 \nabla \phi - \rho_1 g_0 \hat{r} - \nabla(\rho_0 g_0 u_r) + \vec{f}_{\rm td} = 0, \tag{1}$$

where $\vec{\vec{\tau}}$ is the stress tensor, ϕ is the incremental gravitational potential, ρ_0 is the reference density of the mantle, g_0 is the unperturbed gravitational acceleration, u_r is the radial component of displacement, $\rho_1 = -\nabla \cdot (\rho_0 \vec{u})$ is the Eulerian density perturbation (Wu & Peltier 1982) due to tidal deformation and $\vec{f}_{\rm td}$ is the body tide force. The elastic constitutive relation that relates the stress to the displacement is

$$\vec{\vec{\tau}} = \lambda_0 (\nabla \cdot \vec{u}) \vec{\vec{I}} + \mu_0 (\nabla \vec{u} + (\nabla \vec{u})^T), \tag{2}$$

where $\lambda_0(r)$ and $\mu_0(r)$ are the first Lamé parameter and the shear modulus, respectively, from the spherical reference model. The gravitational potential ϕ is governed by Poisson's equation

$$\nabla^2 \phi = 4\pi G \rho_1. \tag{3}$$

The tidal potential in the Moon, caused by the Earth, can be expressed as an infinite series of spherical harmonics of degree l and order m (Agnew 2008), with by far the largest terms occurring at degree $l = 2$. Here, we only consider the degree-2 terms caused by the monthly variation in the Earth–Moon distance due to the Moon's eccentric orbit; that is the terms in Wahr *et al.* (2009) that have a $\cos(nt+\varphi_0)$ temporal signature:

$$V_{\rm td}(r,\theta,\phi,t) = \frac{3\varepsilon G m a^2}{4R^3} \left(\frac{r}{a}\right)^2 \times [(1-3\cos^2\theta) + 3\sin^2\theta \cos(2\phi)] \cos(nt+\varphi_0), \tag{4}$$

where r, θ, ϕ and t are the spherical coordinates and the time, respectively, ε is the lunar orbital eccentricity, a is the Moon's radius, R is the semi-major axis, m is the mass of the Earth, $n = \frac{2\pi}{T}$ where T is the orbital period and φ_0 is the initial phase. Note that for an elastic body, the tidal response must have the same $\cos(nt+\varphi_0)$ time dependence as the applied tidal force.

This tidal potential in eq. (4) does not include contributions from the librational tide: that is tidal forcing caused by the fact that for an eccentric orbit the Moon does not keep exactly the same face pointed towards the Earth, but rocks back and forth relative to the Earth–Moon vector. The librational tide has a $\sin(nt+\varphi_0)$

Downloaded from http://gji.oxfordjournals.org/ at University of Colorado on August 29, 2014

time dependence, and is of the same order as the terms shown in eq. (4). Our purpose here, though, is simply to describe and assess a new semi-analytic method of computing the tidal effects of laterally heterogeneous structure, and this does require we use a complete description of the tidal potential. So, we have omitted the librational tidal forcing, for simplicity.

Hereafter, we ignore the time-dependent coefficient $\cos(nt + \varphi_0)$ and eq. (4) is simplified to

$$V_{\rm td}(r, \theta, \phi) = r^2(Z_1 Y_{20} + Z_2 Y_{22}), \tag{5}$$

where Y_{20} and Y_{22} are the real-form spherical harmonic functions of degree $l = 2$, order $m = 0$ and $m = 2$ [i.e., (2, 0) and (2, 2)], respectively (see Appendix A for the definition of Y_{lm}), and where $Z_1 = -\sqrt{\frac{9\pi}{5}}\frac{\varepsilon G m}{R^3}$ and $Z_2 = -\sqrt{3}Z_1$ are constant coefficients. Below, we will sometimes consider the (2, 0) or (2, 2) tidal forcing cases separately. The tidal force is given by

$$\vec{f}_{\rm td} = -\rho_0 \nabla V_{\rm td}. \tag{6}$$

2.2 Perturbation theory

Eqs (1)–(3), when accompanied by appropriate continuity conditions, can be solved semi-analytically to determine the body-tide-induced displacement $\vec{u}_0$ and gravitational potential ϕ_0 for a spherically symmetric planetary mantle (e.g. Farrell 1972; Tromp & Mitrovica 1999). We express that spherically symmetric solution as $(\vec{u}_0, \phi_0)$ for brevity. When there are small lateral heterogeneities in the elastic moduli in the planet's mantle, eqs (1)–(3) are modified and solving them becomes more complicated. Using a perturbation method, we reformulate the modified eqs (1)–(3) by treating the lateral heterogeneities in the elastic properties as a perturbation, and reorganize the differential equations in terms of different orders of the perturbation. In this paper, we consider effects of lateral heterogeneities only in the shear modulus, and we assume they have a laterally varying pattern described by a specific spherical harmonic of degree l and order m,

$$\delta\mu(r, \theta, \phi) = \zeta(r)\mu_0(r)Y_{lm}(\theta, \phi), \tag{7}$$

where $\mu_0(r)$ is the reference shear modulus, $Y_{\rm lm}$ is the real-form spherical harmonic function at (l, m) and $\zeta(r)$ is the relative amplitude of the lateral variability, which is chosen below to be either constant through the entire mantle, or constant through an individual shell of the mantle and zero outside that shell. Including this lateral heterogeneity in the shear modulus, the constitutive relation, eq. (2), becomes

$$\overleftrightarrow{\tau} = \lambda_0(\nabla \cdot \vec{u})\overleftrightarrow{I} + (\mu_0 + \delta\mu)[\nabla\vec{u} + (\nabla\vec{u})^T]. \tag{8}$$

Replacing $\overleftrightarrow{\tau}$ in eq. (2) with that in eq. (8) leads to a set of slightly modified differential equations, and we denote the corresponding tidal response solution as $(\vec{u}, \phi)$. From the perturbation theory point of view (e.g. Richards & Hager 1989), if the perturbation is small (i.e. $\zeta \ll 1$), $(\vec{u}_0, \phi_0)$ is slightly modified to $(\vec{u}, \phi) = (\vec{u}_0 + \vec{u}', \phi_0 + \phi')$, where $(\vec{u}', \phi')$ represents the small modification to $(\vec{u}_0, \phi_0)$ due to $\delta\mu$. We call $(\vec{u}_0, \phi_0)$ the zeroth-order solution and $(\vec{u}', \phi')$ the high-order residual. We further write $(\vec{u}', \phi') = (\vec{u}_1, \phi_1) + (\vec{u}_2, \phi_2) + (\vec{u}'', \phi'')$, where $(\vec{u}_1, \phi_1)$ and $(\vec{u}_2, \phi_2)$ are the first- and second-order (in the amplitude, ζ, of the lateral heterogeneity) corrections to $(\vec{u}_0, \phi_0)$, respectively, and $(\vec{u}'', \phi'')$ is the combined correction from all higher orders. This expansion to $(\vec{u}', \phi')$ could be extended to third- and higher-orders, but a truncation at second order is sufficient for the range of values of ζ considered below.

We re-write eqs (1) and (3), combined with eq. (8), into three separate groups of differential equations, representing the equations for the zeroth, first, and second orders of the perturbation, respectively. These three sets of equations have the same general form, which can be expressed as follows,

$$\begin{cases} \nabla \cdot [\lambda_0(\nabla \cdot \vec{u}_D)\overleftrightarrow{I} + \mu_0(\nabla\vec{u}_D + (\nabla\vec{u}_D)^T)] \\ \quad - \rho_0\nabla\phi_D + \nabla \cdot (\rho_0\vec{u}_D)g_0\hat{r} - \nabla(\rho_0 g_0 u_{Dr}) = -\mathcal{F}_D \ , \\ \nabla^2\phi_D = -4\pi G\nabla \cdot (\rho_0\vec{u}_D) \end{cases} \tag{9}$$

where the subscript D denotes the order of the perturbation, that is $D = 0$, 1 or 2, $\mathcal{F}_D$ is the effective forcing term and is different for different orders of the perturbation. Specifically, when $D = 0$, $\mathcal{F}_0$ is just the tidal force and $\mathcal{F}_0 = \vec{f}_{\rm td}$. When $D = 1$ or 2, $\mathcal{F}_D = \nabla \cdot (\delta\mu[\nabla\vec{u}_{D-1} + (\nabla\vec{u}_{D-1})^T])$, and the equations are forced by the coupling between $\delta\mu$ and the lower-order displacement field $\vec{u}_{D-1}$.

To solve eq. (9) for each order of the perturbation, appropriate continuity conditions are needed at the core–mantle boundary (CMB), the outer surface, and any internal boundary in the mantle. At any solid–solid spherical internal boundary, the normal traction $\hat{r} \cdot \overleftrightarrow{\tau}_D$, the displacement $\vec{u}_D$, the incremental potential ϕ_D and the normal component of the adjusted incremental gravitational acceleration $\hat{r} \cdot (\nabla\phi_D + 4\pi G\rho_0\vec{u}_D)$ are continuous, expressed as

$$[\hat{r} \cdot \overleftrightarrow{\tau}_D]^+_- = [\vec{u}_D]^+_- = [\phi_D]^+_- = [\hat{r} \cdot (\nabla\phi_D + 4\pi G\rho_0\vec{u}_D)]^+_- = 0, \tag{10}$$

where $[]^+_-$ denotes the jump of the enclosed quantity from the lower $(-)$ to the upper $(+)$ side of an interface, $\hat{r}$is the unit vector in the radial direction (it enters into these equations because it is the normal to spherical boundaries) and $\overleftrightarrow{\tau}_D$ is the stress tensor for order D of the perturbation. The radial traction is

$$\hat{r} \cdot \overleftrightarrow{\tau}_D = \hat{r} \cdot \left(\lambda_0(\nabla \cdot \vec{u}_D)\overleftrightarrow{I} + \mu_0\left[\nabla\vec{u}_D + (\nabla\vec{u}_D)^T\right]\right) + \mathcal{B}_D, \tag{11}$$

where $\mathcal{B}_D = \Theta(D)\hat{r} \cdot [\delta\mu(\nabla\vec{u}_{D-1} + (\nabla\vec{u}_{D-1})^T)]$, and $\Theta(D) = 0$ when $D = 0$ and $\Theta(D) = 1$ when $D = 1$ or 2 (i.e. a non-vanishing $\mathcal{B}_D$ exists in the radial traction, only in the first- and second-order equations). The continuity conditions at the CMB and the outer surface, however, cannot be fully described by eq. (10), and are given in matrix form in eqs (A27) and (A32) in Appendix B.

By comparing the zeroth-order equations and the associated boundary conditions with those of the high-order equations, the only differences are the two terms, $\mathcal{F}_D$ and $\mathcal{B}_D$. The zeroth-order motion is driven solely by the tidal force, while the first- and second-order motions are both driven by an effective force, together with an inhomogeneous term in the radial traction continuity condition. We call $\mathcal{F}_D$ and $\mathcal{B}_D$ in the high-order equations the high-order forcing terms or, later, the coupling terms.

The solution to the zeroth-order equations ($D = 0$) is the tidal response of a spherically symmetric planet. The spherical response to any given force is described with the same spherical harmonics that are present in that force. Since in our case the tidal force $\vec{f}_{\rm td}$ consists solely of the spherical harmonics (2, 0) and (2, 2) (see eq. 5), those are the harmonics that enter into the zeroth-order response. We refer to this zeroth-order tidal response as the primary response.

The solution to the high-order equations represents the response of a spherically symmetric planet to the high-order forcing terms, $\mathcal{F}_D$ and $\mathcal{B}_D (D = 1$ or 2). Thus, these solutions are described with

Downloaded from http://gji.oxfordjournals.org/ at University of Colorado on August 29, 2014

the same harmonics that enter into those forcing terms. The first-order response includes harmonics other than (2, 0) and (2, 2), since the forcing terms couple the (2, 0) and (2, 2) harmonics in $\vec{u}_0$ with the harmonics in $\delta\mu$. Similarly, the second-order response results from the coupling of $\vec{u}_1$ and $\delta\mu$, and spans an even larger set of harmonics than those in the first-order response. We refer to the first- and second-order responses as the high-order (or secondary) response.

In the next section, we convert eq. (9) and its boundary conditions eq. (10) into matrix forms, illustrate the mode coupling process, and present solution strategies for the matrix equations to obtain the zeroth-, first- and second-order responses.

3 METHOD

3.1 Equations in matrix form

To solve for the tidal response, it is convenient to reformulate eqs (9) and (10) into a matrix form (Wu & Peltier 1982; Tromp & Mitrovica 1999) that permits propagator matrix solution techniques. The mathematical procedure of converting the zeroth-order equations into matrix form is well developed (e.g. Dahlen & Tromp 1998). A similar procedure is applied here to the high-order equations. We expand the incremental potential ϕ into spherical harmonics, while expanding the displacement $\vec{u}$ and the non-coupling terms in the radial traction $\hat{r}\cdot\overleftrightarrow{\tau}$ into vector spherical harmonics (VSH; see Appendix B), as follows:

$$\vec{u}_D = \sum_{l,m}\left(U^D_{lm}\vec{P}_{lm} + V^D_{lm}\vec{B}_{lm} + W^D_{lm}\vec{C}_{lm}\right), \tag{12}$$

$$\phi_D = \sum_{l,m} K^D_{lm} Y_{lm}, \tag{13}$$

$$\hat{r}\cdot\left(\lambda_0(\nabla\cdot\vec{u}_D)\overleftrightarrow{I} + \mu_0\left[\nabla\vec{u}_D + (\nabla\vec{u}_D)^T\right]\right) = \sum_{l,m}\left(R^D_{lm}\vec{P}_{lm} + S^D_{lm}\vec{B}_{lm} + T^D_{lm}\vec{C}_{lm}\right), \tag{14}$$

where $\vec{P}_{lm}$, $\vec{B}_{lm}$ and $\vec{C}_{lm}$ are the orthogonal bases of the VSH expansion. The expansion coefficients in eq. (14) are

$$R^D_{lm} = (\lambda_0 + 2\mu_0)\dot{U}^D_{lm} + \frac{\lambda_0}{r}\left(2U^D_{lm} - l(l+1)V^D_{lm}\right), \tag{15}$$

$$S^D_{lm} = \mu_0\left(\dot{V}^D_{lm} - \frac{V^D_{lm}}{r} + \frac{U^D_{lm}}{r}\right), \tag{16}$$

$$T^D_{lm} = \mu_0\left(\dot{W}^D_{lm} - \frac{W^D_{lm}}{r}\right), \tag{17}$$

where a dot denotes d/dr. Note that U^D_{lm}, V^D_{lm}, W^D_{lm}, R^D_{lm}, S^D_{lm} and T^D_{lm} are functions of r, while the angular dependence is present in Y_{lm}, $\vec{P}_{lm}$, $\vec{B}_{lm}$ and $\vec{C}_{lm}$.

The forcing terms $\mathcal{F}_D$ in eq. (9) and $\mathcal{B}_D$ in eq. (11) also need to be expanded into VSH. For the zeroth-order equations, $\mathcal{B}_0 = 0$ and $\mathcal{F}_0 = \vec{f}_{\rm td}$. The VSH expansion of $\vec{f}_{\rm td}$ is straightforward, and is given by eq. (A20). For the high-order equations ($D = 1$ or 2), $\mathcal{F}_D$ and $\mathcal{B}_D$ refer to the coupling terms. Physically, these coupling terms demonstrate the mode coupling between the shear modulus heterogeneities and the lower-order (i.e. order D-1) tidal deformation field, and lead to a response of order D at predictable harmonic modes. The VSH expansion of the coupling terms, derived in Appendix A, is:

$$\mathcal{F}_D = \sum_{l,m}\left(F^{p,D}_{lm}\vec{P}_{lm} + F^{b,D}_{lm}\vec{B}_{lm} + F^{c,D}_{lm}\vec{C}_{lm}\right), \tag{18}$$

$$\mathcal{B}_D = \Theta(D)\sum_{l,m}\left(R^{\rm cp,D}_{lm}\vec{P}_{lm} + S^{\rm cp,D}_{lm}\vec{B}_{lm} + T^{\rm cp,D}_{lm}\vec{C}_{lm}\right). \tag{19}$$

We discuss the mode coupling process in the next subsection.

We introduce another auxiliary variable

$$Q^D_{lm} = \dot{K}^D_{lm} + \frac{l+1}{r}K^D_{lm} + 4\pi G\rho_0 U^D_{lm}, \tag{20}$$

which is related to the incremental gravitational acceleration. Substituting eqs (12)–(20) into eqs (9)–(11) for each order D yields two decoupled sets of ordinary differential equations along with boundary conditions. The two sets of equations represent two individual modes of motion, the spheroidal (s) and the toroidal (t) modes, and can be solved separately. Both sets of equations can be written in the same general matrix form for each harmonic (l, m), as

$$\frac{d\boldsymbol{X}^D_{lm}}{{\rm d}r} = \boldsymbol{A}_l\boldsymbol{X}^D_{lm} - \boldsymbol{F}^D_{lm}, \tag{21}$$

where $\boldsymbol{X}^D_{lm}$ is the solution vector for harmonic (l, m), $\boldsymbol{A}_l$ is a square matrix and depends on the harmonic degree l but not on the order m and $\boldsymbol{F}^D_{lm}$ is the vector form of the expansion of the coupling term $\mathcal{F}_D$. The forms of $\boldsymbol{X}$, $\boldsymbol{A}$ and $\boldsymbol{F}$ depend on whether the coupling term excites a spheroidal mode or a toroidal mode (here, and throughout the remainder of this paper, the subscripts denoting the spherical harmonic (l, m), and the superscripts/subscripts D denoting the order of the perturbation, are omitted for simplicity). For a spheroidal mode, eq. (21) is 6-by-6 and $\boldsymbol{X}$ has six components, while for a toroidal mode, eq. (21) is 2-by-2 and $\boldsymbol{X}$ has two components. The explicit forms of $\boldsymbol{X}$, $\boldsymbol{A}$, $\boldsymbol{F}$ and the associated boundary conditions at the CMB, the outer surface, and any internal boundary are given in Appendix B for both the spheroidal and toroidal modes. In addition, all the physical quantities in eq. (21) are non-dimensionalized in order to solve the equations more conveniently.

3.2 Mode coupling

Mode coupling generates the high-order (or secondary) responses. Based on eqs (9) and (11), the coupling of the lateral heterogeneity $\delta\mu$ and the degree-2 primary response gives rise to the first-order response, while the further coupling of $\delta\mu$ with the first-order response leads to the second-order response. Here, we call the lower-order (i.e. order D-1) mode (response) the parent mode (response), and the higher-order (i.e. order D) mode (response) that results from the coupling as the child mode (response).

The VSH expansion of the coupling terms $\mathcal{F}$ and $\mathcal{B}$ makes it possible to determine the harmonic modes that are present in the first- and second-order solutions, before actually solving the differential equations (see Appendix A). For the following, we suppose that $\delta\mu$ is at harmonic (l_1, m_1) and the parent response (spheroidal or toroidal) is at harmonic (l_0, m_0). These combine into $\mathcal{F}$ and $\mathcal{B}$, and separate into individual spheroidal (s) and toroidal (t) coupling terms at a few harmonics (l, m). Because the high-order equations are spherically symmetric, each spheroidal (or toroidal) coupling term will induce exactly the same spheroidal (or toroidal) mode in the response, denoted here as $s(l, m)$ [or $t(l, m)$].

We categorize the mode coupling process into four types of parent–child mode pairings: s to s, s to t, t to s and t to t, and

Downloaded from http://gji.oxfordjournals.org/ at University of Colorado on August 29, 2014

we summarize these processes into generalized selection rules that can be described by

$$
\begin{aligned}
&\text{if } sign(m_0)\cdot sign(m_1) > 0\\
&p(l_0,m_0)\otimes(l_1,m_1) \Rightarrow \begin{cases} p(l,m),(l,m)\in \mathcal{L}_1\otimes\mathcal{M}_1\\ \bar{p}(l,m),(l,m)\in \mathcal{L}_2\otimes\mathcal{M}_2\end{cases}\\
&\text{if } sign(m_0)\cdot sign(m_1) < 0\\
&p(l_0,m_0)\otimes(l_1,m_1) \Rightarrow \begin{cases} p(l,m),(l,m)\in \mathcal{L}_1\otimes\mathcal{M}_2\\ \bar{p}(l,m),(l,m)\in \mathcal{L}_2\otimes\mathcal{M}_1\end{cases}\\
&\text{where } sign(x) = \begin{cases} 1 & x\geq 0\\ -1 & x<0\end{cases}\text{, and,}\\
&\mathcal{L}_1 : l = |l_0-l_1|+2i,\ 0\leq i\leq \tfrac{1}{2}(l_0+l_1-|l_0-l_1|),\ i \text{ is integer}\\
&\mathcal{L}_2 : l = |l_0-l_1|+2i+1,\ 0\leq i\leq \tfrac{1}{2}(l_0+l_1-|l_0-l_1|)-1,\\
&i \text{ is integer } (l_0\neq 0, l_1\neq 0)\\
&\mathcal{M}_1 : m = ||m_0|-|m_1|| \text{ or } ||m_0|+|m_1||\text{, and } |m|\leq l\\
&\mathcal{M}_2 : m = -||m_0|-|m_1|| \text{ or } -||m_0|+|m_1||,\ |m|\leq l, \text{and m}\neq 0,
\end{aligned}
\tag{22}
$$

where p denotes the s (or t) mode and $\bar{p}$ denotes the other mode, that is the t (or s) mode, $\mathcal{L}_1$,$\mathcal{L}_2$,$\mathcal{M}_1$ and $\mathcal{M}_2$ are the sets of the harmonic degrees and orders that are allowed by the selection rules.

While the selection rules predict the harmonic modes caused by the coupling, the radially dependent expansion coefficients (i.e. F^p,F^b,F^c,$R^{\rm cp}$,$S^{\rm cp}$ and $T^{\rm cp}$) in the coupling terms govern the strength of the coupling, and are expressed by eqs (A12)–(A19) in Appendix A. The amplitude of each mode in the tidal response depends on the amplitude, ζ, of the lateral variability. Specifically, the amplitude of the first-order response is linearly proportional to ζ, while the amplitude of the second-order response is a quadratic function of ζ.

3.3 Semi-analytic approach and solutions

Given the matrix forms of eq. (21) and the associated boundary conditions, the tidal response for each order of the perturbation can be solved mode by mode using the propagator matrix method together with a Runge–Kutta numerical scheme (see Appendix C). For numerical implementation of the propagator matrix method, we set up a 1-D radial grid that has a fine-enough resolution to ensure convergence of the Runge–Kutta solution. We make sure that there are two gridpoints at each radial discontinuity in material properties. We also make sure that there are two gridpoints at each radial discontinuity of $\delta\mu$, so that we can apply the appropriate boundary conditions at those discontinuities (see Appendix C for more description).

The basic idea of the propagator matrix method is that, given the explicit form of eq. (21) and a starting solution $\boldsymbol{X}(r_0)$ at radius r_0 in the mantle, the solution $\boldsymbol{X}(r)$ at any radius r can be determined by successively propagating $\boldsymbol{X}(r_0)$ from r_0 to r. To simplify our solution method, we start the propagation from the CMB (i.e. $r=r_{\rm c}$) instead of from the centre of the inner core (i.e. $r=0$), and the starting solution $\boldsymbol{X}(r_{\rm c})$ is partly unknown (see eqs A27 and A32). Such simplification proves to produce little inaccuracy to our calculations. Only a ∼0.1 per cent level difference is found when comparing our solutions with those calculated using the classical methods that include a core, for 1-D planetary models with varying core sizes. To fully determine $\boldsymbol{X}(r_{\rm c})$, we propagate it to the outer surface (i.e. $r=r_{\rm s}$), imposing the appropriate boundary conditions as we pass across internal discontinuities, and equate the resulting undetermined solution to the outer surface boundary value $\boldsymbol{X}(r_{\rm s})$ (also see eqs A27 and A32). By solving a linear equation relating the unknowns in $\boldsymbol{X}(r_{\rm c})$ and $\boldsymbol{X}(r_{\rm s})$, we are able to solve for $\boldsymbol{X}(r_{\rm c})$ and $\boldsymbol{X}(r_{\rm s})$ and determine the solution, $\boldsymbol{X}(r_i)$, at any gridpoint r_i (see eq. A45). Once we have solved the order $D-1$ equations, we use these solutions to construct the order D coupling terms and solve the resulting order D equations using the same procedure.

It is conceivable that some planetary bodies, including possibly even the Moon, might not possess a fluid core, in which case there would be no CMB to start the propagation from. For such a body, however, we can circumvent this problem by inserting a very small fluid core at the centre of the planet, and starting our solutions at the surface of that small sphere.

For the special case of the high-order degree-1 spheroidal mode, an unconstrained translational motion associated with a rigid shift of the planet is contained in the solution to eq. (21), and needs to be subtracted to obtain the degree-1 response (Farrell 1972). The translational mode satisfies the homogeneous form of eq. (21), and its unit form can be expressed as

$$\boldsymbol{X}^{\rm tr}(r) = [1,\,1,\,0,\,0,\,-g(r),\,0]^T, \tag{23}$$

where $g(r)$ is the gravitational acceleration at radius r. Note that in the centre of mass reference frame we consider here, the degree-1 response must have zero gravitational potential at the outer surface. This condition is applied to determine the degree-1 response by adding a multiple of eq. (23) to the solution to eq. (21), to obtain

$$\boldsymbol{X}^{\rm net}(r) = \boldsymbol{X}(r) + \alpha\cdot\boldsymbol{X}^{\rm tr}(r), \tag{24}$$

where $\alpha = K(r_{\rm s})/g(r_{\rm s})$, $r_{\rm s}$ is the Moon's radius and $\boldsymbol{X}^{\rm net}(r)$ is the actual degree-1 response in the centre of mass reference frame (Farrell 1972).

4 RESULTS

We apply the perturbation method described above to solve for the tidal response of the Moon. The Moon is modelled with a solid inner core, a fluid outer core and seven mantle and crust layers of different properties, according to a recent lunar seismic study (Table 1). In our calculations, we adopt this seismic model, and refer to the top seven layers as the lunar 'mantle'. We assume for most of our calculations that there are long-wavelength lateral heterogeneities in the shear modulus throughout some prescribed depth range of the lunar mantle. For most, though not all, of these calculations we assume that the heterogeneities can be represented by a (1, 1) harmonic, since that best represents a nearside-farside asymmetric structure.

Table 1. Lunar model parameters (Weber *et al.* 2011).

Depths (km)	ρ_0 (kg m^{-3})	V_p (km s^{-1})	V_s (km s^{-1})
0–15	2700	3.2	1.8
15–40	2800	5.5	3.2
40–238	3300	7.7	4.4
238–488	3400	7.8	4.4
488–738	3400	7.6	4.4
738–1257	3400	8.5	4.5
1257–1407	3400	7.5	3.2
1407–1497 (outer core)	5100	4.1	0.0
1497–1740 (inner core)	8000	4.3	2.3
Semi-major axis, R		3.844×10^8 m	
Eccentricity, ε		0.0549	
Earth's mass, m		5.97×10^{24} kg	
Moon's radius, a		1.74×10^6 m	

Downloaded from http://gji.oxfordjournals.org/ at University of Colorado on August 29, 2014

We calculate the tidal response of the Moon for three scenarios regarding the choice of lateral heterogeneities: (1) a (1, 1) harmonic pattern throughout the entire mantle, (2) a (1, 1) harmonic pattern in either the bottom or the top half of the mantle, (3) other long-wavelength patterns of harmonic (l_1, m_1) throughout the mantle. We apply the (2, 0) and (2, 2) tidal force components separately for the first two scenarios, but apply the sum of those two components (i.e., eq. 5 for the total tidal potential) for the third scenario. We calculate the full set of first- and second-order responses for both the spheroidal and torodial modes. However, we present the results primarily for the spheroidal modes, since only the spheroidal modes contribute to the radial displacement and the gravitational potential, which are the quantities that can be inferred using observations from current space missions. Note that toroidal modes, when coupled with laterally heterogeneous structure, can induce higher-order spheroidal motions. For each high-order spheroidal response $s(l, m)$ at order D, we define the relative tidal response using the normalized radial displacement $h^D_{lm} = U^D_{lm}(a)/U^0_{\rm td}(a)$ and the normalized gravitational potential $k^D_{lm} = K^D_{lm}(a)/K^0_{\rm td}(a)$ at the lunar surface, where $U^0_{\rm td}(a)$ and $K^0_{\rm td}(a)$ are the associated primary responses at degree 2. We also compute the tidal response for the same model using the finite element code CitcomSVE (Zhong *et al.* 2012), and compare the results from the perturbation method with those from the finite element method.

4.1 (1, 1) lateral heterogeneities throughout the mantle

We define the harmonic (1, 1) lateral heterogeneity in μ as

$$\delta\mu = \zeta \cdot \mu_0 \cdot Y_{11} = -\Delta \cdot \mu_0 \sin\theta \cos\phi, \tag{25}$$

where ζ is a non-zero constant throughout the mantle, and $\Delta = \sqrt{\frac{3}{4\pi}}\zeta$ is the peak amplitude of the lateral variability in the shear modulus. The value of Δ is chosen to vary from 2.5 to 40 per cent, so that it spans a large range of perturbations. (The upper values of this range are larger than what we would expect for the real Moon.)

Using our perturbation method, we first determine the high-order response modes from our mode coupling analysis, for (2, 0) and (2, 2) tidal forcing separately (see Fig. 1). We define the harmonic (l, m) spheroidal (toroidal) mode of perturbation order D as $s^D(l, m)$ $[t^D(l, m)]$. A (2, 0) tidal force induces a $s^0(2, 0)$ primary response. Based on our selection rules in eq. (22), the coupling of $s^0(2, 0)$ with the (1, 1) lateral heterogeneity gives rise to a first-order response consisting of two spheroidal modes $s^1(1, 1)$ and $s^1(3, 1)$ and one toroidal mode $t^1(2, -1)$. These first-order modes couple with the (1, 1) structure to excite second-order responses that span harmonic degrees 2 to 4. In particular, all three first-order modes excite $s^2(2, 0)$ and $s^2(2, 2)$, while $s^1(3, 1)$ generates additional degree-4 spheroidal modes, which are $s^2(4, 0)$ and $s^2(4, 2)$. For (2, 2) tidal forcing, the same three first-order modes are generated as for (2, 0) tidal forcing, along with an additional $s^1(3, 3)$ mode. Thus, the harmonic content of the second-order response to (2, 2) forcing includes all the same harmonics as for (2, 0) forcing, plus the harmonics that derive from the $s^1(3, 3)$ mode. Those latter harmonics include $s^2(4, 4)$ and an additional $s^2(2, 2)$ contribution (note that $s^1(3, 3)$ does not induce a $s^2(2, 0)$ term). Though the responses to (2, 0) and (2, 2) forcing have nearly the same high-order mode content, the amplitude of each mode differs in the two cases. Note that the amplitude of the same mode from different couplings need to be summed together to obtain the total amplitude of that mode.

We calculate the relative response of the radial displacement h_{lm} and the gravitational potential k_{lm}, of all the high-order spheroidal modes for different values of Δ, and show the absolute values of the results in Figs 2(a) and (b) for (2, 0) forcing, and in Figs 2(c) and (d) for (2, 2) forcing. The response amplitudes of the first-order modes, that is $s^1(1, 1)$ and $s^1(3, 1)$ for the (2, 0) tidal forcing, and $s^1(1, 1)$, $s^1(3, 1)$ and $s^1(3, 3)$ for the (2, 2) tidal forcing, increase linearly with Δ, while the amplitudes of the second-order modes, that is $s^2(2, 0)$, $s^2(2, 2)$, $s^2(4, 0)$ and $s^2(4, 2)$ for the (2, 0) tidal forcing, and $s^2(2, 0)$, $s^2(2, 2)$, $s^2(4, 0)$, $s^2(4, 2)$ and $s^2(4, 4)$ for the (2, 2) tidal forcing, are quadratic functions of Δ. Note that the degree-1 responses in the gravitational potential are zero in the centre of mass reference (see eq. 24).

For relatively weak perturbations (i.e. small Δ), the first-order responses are generally orders of magnitude stronger than those of second order (Fig. 2). However, due to their quadratic dependence on Δ, the second-order responses become increasingly significant with increasing Δ, and some of them approach or exceed the first-order responses at large Δ (>20 per cent; Fig. 2). We take $s^2(2, 0)$ induced by the (2, 0) tidal forcing and $s^2(2, 2)$ induced by the (2, 2) tidal forcing (i.e. the 'self-coupling' modes) as examples. When Δ is as large as 40 per cent, the $s^2(2, 0)$ gravitational potential response, $k^2_{2,0}$, is 70 per cent of the associated $s^1(3, 1)$ response, while the $s^2(2, 2)$ gravitational potential response, $k^2_{2,2}$, is 53 per cent of the associated $s^1(3, 3)$ response and is 113 per cent greater than the $s^1(3, 1)$ response (Fig. 2). We also find that these self-coupling responses are always one order of magnitude stronger than the other second-order responses, on average. This happens because these second-order self-coupling responses are generated through a forward-and-backward mode coupling process. More specifically, if a child mode $s^D(l, m)$ from the forward coupling of $s^{D-1}(l_0, m_0) \otimes (l_1, m_1) \rightarrow s^D(l, m)$ has the same (or opposite) sign as its parent mode $s^{D-1}(l_0, m_0)$, then the backward coupling

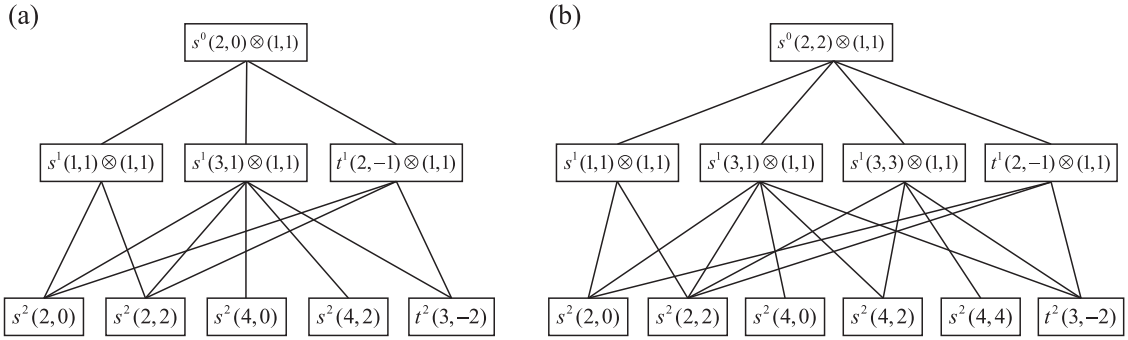

Figure 1. Diagrams of the mode couplings (up to second order in the perturbation) between a spherical harmonic (1, 1) laterally heterogeneous structure in shear modulus and the (a) (2, 0) and (b) (2, 2) tidal forces, respectively, based on the selection rules in eq. (22). In both diagrams, *s* and *t* represent spheroidal and toroidal modes, respectively. The superscript 0, 1 and 2 denote the primary (i.e. zeroth order), the first-order and the second-order modes, respectively.

Downloaded from http://gji.oxfordjournals.org/ at University of Colorado on August 29, 2014

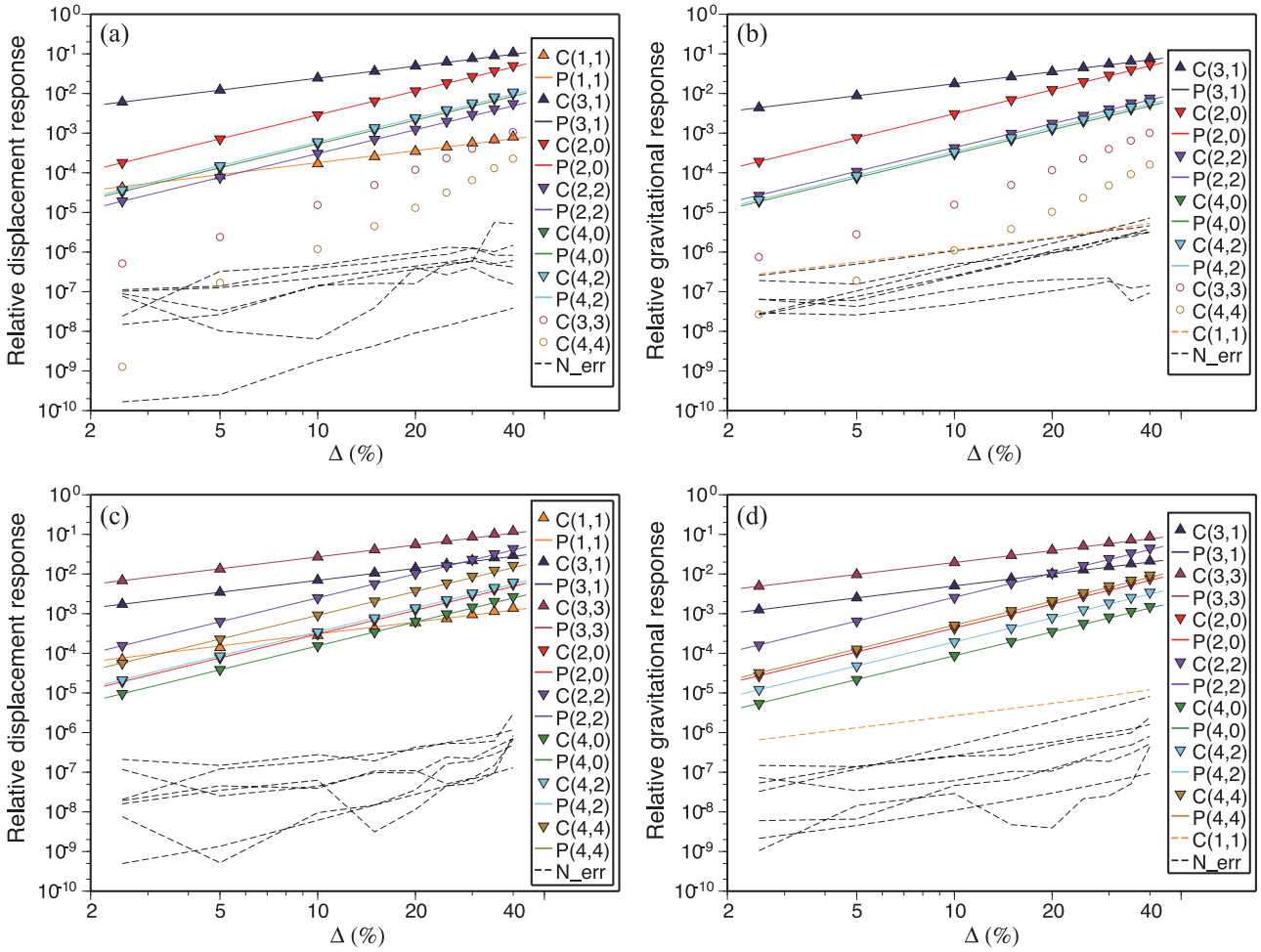

Figure 2. Log–log plots of the absolute values of the relative responses for a Moon with (1, 1) lateral heterogeneities in shear modulus, to (2, 0) (a and b) and (2, 2) (c and d) tidal forces. The amplitude of the lateral variability in the shear modulus is represented by Δ, and the results are shown for Δ from 2.5 to 40 per cent. The relative responses in the surface radial displacement (a and c) and the surface gravitational potential (b and d) are shown, respectively, for each spheroidal harmonic mode $s(l, m)$ from the mode couplings. The straight solid lines represent the response modes predicted by our second-order perturbation method (denoted by P). The triangles (first order), inverted triangles (second order) and open circles (higher than second order) represent results computed using CitcomSVE, that we believe to be correct (denoted by C). The dashed lines are also results from CitcomSVE calculations for all the other harmonics of $0 \leq l \leq 4$ and $0 \leq m \leq l$, and are believed to be numerical noise (denoted by N_err). Note that k_{11} from CitcomSVE (b and d) are highlighted.

$s^D(l, m) \otimes (l_1, m_1) \rightarrow s^{D+1}(l_0, m_0)$ must generate a $s^{D+1}(l_0, m_0)$ mode that also has the same (or opposite) sign as $s^D(l, m)$. Therefore, the self-coupling responses always have the same sign as their primary response, which may not be true for the other second-order responses. Since it is guaranteed that the contributions from all the first-order modes to the self-coupling modes add constructively, the self-coupling response is always the largest among the second-order responses.

We also compute the tidal responses numerically using the finite element code CitcomSVE (Zhong *et al.* 2003; A *et al.* 2013). In CitcomSVE, the mantle is modelled as a series of spherical shells overlying a fluid core, and the combined volume of those shells is divided into 12×48^3 elements. The same 1-D model of the lunar mantle is used in CitcomSVE as in the perturbation method. Here, the tidal response is quantified by h_{lm} and k_{lm}, which are the spherical harmonic expansion coefficients of the surface radial displacement field and surface gravitational potential field, respectively. h_{lm} and k_{lm} are determined for harmonic degrees and orders of $0 \leq l \leq 4$ and $0 \leq m \leq l$ in this scenario, and are normalized (i.e. relative response) in the same way as in our perturbation calculations. Note that, when lateral heterogeneities are added into the numerical model, h_{lm} and k_{lm} are obtained by subtracting the 1-D response (i.e. without heterogeneities) from the 3-D response (i.e. with heterogeneities), in order to suppress the numerical errors that may be significant at very small perturbations. By comparing the CitcomSVE results with those from the perturbation method, we categorize the numerical results into three types: (1) those that are correct and are predicted by our second-order perturbation method (triangles in Fig. 2), (2) those that are probably correct but that are not predicted by our perturbation method (open circles in Fig. 2) and (3) those that are probably caused by numerical noise (dashed lines in Fig. 2).

We find that the most significant responses from CitcomSVE are all predicted by our perturbation method, and that they agree remarkably well with those from the perturbation method (both in their amplitude and in their linear or quadratic dependence on Δ, see Fig. 2) for small and moderate values of Δ. As shown in Table 2, when Δ = 10 per cent, the relative difference between the h_{lm} (or k_{lm}) values of the two methods is no greater than 1 per cent for all non-degree-1 responses. The degree-1 responses h_{11} from

Downloaded from http://gji.oxfordjournals.org/ at University of Colorado on August 29, 2014

Table 2. Comparisons of h and k between the results from the perturbation method and those from the finite element methods, for $\Delta = 10$ per cent.

	I[a]		II		III	
Mode[b]	ε_h (per cent)[c]	ε_k (per cent)	ε_h (per cent)	ε_k (per cent)	ε_h (per cent)	ε_k (per cent)
$s^1(1, 1)_{(2,0)}$	5.56	N/A	10.1	N/A	1.46	N/A
$s^1(3, 1)_{(2,0)}$	0.51	0.51	0.31	0.33	0.36	0.33
$s^2(2, 0)_{(2,0)}$	0.48	0.48	0.10	0.10	0.06	0.04
$s^2(2, 2)_{(2,0)}$	0.59	0.65	0.19	0.26	0.65	0.57
$s^2(4, 0)_{(2,0)}$	0.58	0.19	0.23	0.51	0.13	0.15
$s^2(4, 2)_{(2,0)}$	0.74	0.70	0.12	0.12	0.63	0.51
$s^1(1, 1)_{(2,2)}$	8.82	N/A	9.14	N/A	0.94	N/A
$s^1(3, 1)_{(2,2)}$	0.28	0.26	0.34	0.50	0.24	0.17
$s^1(3, 3)_{(2,2)}$	0.49	0.45	0.28	0.32	0.41	0.34
$s^2(2, 0)_{(2,2)}$	0.64	0.51	0.46	0.81	0.26	0.28
$s^2(2, 2)_{(2,2)}$	0.41	0.42	0.33	0.35	0.62	0.53
$s^2(4, 0)_{(2,2)}$	0.46	0.51	0.34	0.49	0.35	0.21
$s^2(4, 2)_{(2,2)}$	0.44	0.26	0.66	0.70	0.48	0.27
$s^2(4, 4)_{(2,2)}$	0.77	0.82	0.33	0.44	0.66	0.64

[a]Lateral heterogeneity in: I, the entire mantle; II, the bottom half of mantle; III, the top half of mantle.
[b]Spheroidal response of harmonic (l, m), to the (2, 0) and (2, 2) tidal forcing, respectively.
[c]Relative difference $\varepsilon_X = \left|(X_{\text{Citcom}} - X_{\text{pert}})/X_{\text{pert}}\right|$.

CitcomSVE show a ∼10 per cent deviation from those computed using the perturbation method, although $h^1_{1,1}$ is small. This deviation may be attributed to numerical errors in CitcomSVE. We notice that although the gravitational potential response $k^1_{1,1}$ should be zero by definition, the k_{11} results from CitcomSVE display a linear dependence on Δ, and so behave like a first-order response (see Figs 2b and d). The CitcomSVE values for k_{11} are $\sim 10^{-6}$ for $\Delta = 10$ per cent. Considering that the primary response is 1, a $\sim 10^{-6}$ numerical error is small and not unexpected.

The CitcomSVE results gradually deviate from the semi-analytic results as Δ increases, as the perturbation theory suggests. As $\Delta = 20$ per cent, the difference between the numerical results and the semi-analytic results is at the 3 per cent level, for all the first- and second-order modes (i.e. triangles and solid lines in Fig. 2). When Δ is as large as 40 per cent, the differences grow to larger than 10 per cent. This is because for large perturbations, contributions from effects higher than second order become significant in the numerical results, and our second-order perturbation method is unable to predict them. According to our selection rules, the higher-order contributions to the first- and second-order responses start from the third and the fourth orders in the perturbation, respectively, so they grow slowly as Δ increases and are not obvious in Fig. 2 even for large values of Δ. Clear evidence of higher-order ($D > 2$) effects can be seen in Figs 2(a) and (b) [i.e. for (2, 0) forcing], which show significant $s(3, 3)$ and $s(4, 4)$ (open circles) responses in the CitcomSVE results that are not predicted by our second-order theory. As $\Delta \geq 10$ per cent, these $s(3, 3)$ and $s(4, 4)$ responses display approximately cubic and quartic dependence on Δ, implying that they are third- and fourth-order effects, respectively. More specifically, $s^3(3, 3)$ is from the coupling between $s^2(2, 2)$ and (1, 1) structure, while $s^4(4, 4)$ is from further coupling between $s^3(3, 3)$ and (1, 1) structure. However, no such individual higher-order responses are observed for (2, 2) tidal forcing (e.g. Figs 2c and d). This is because all the higher-order effects in that case are coincidently buried in the first- and second-order responses, which are dominant.

Of all the other modes from CitcomSVE (dashed lines in Fig. 2), the h_{lm} and k_{lm} are at a level of 10^{-6} or less and display pseudo-random behavior with respect to increasing Δ. Considering that they are six orders of magnitude smaller than the primary response, and that they are not predicted to exist from our perturbation method, we believe them to be numerical noise. Additionally for (2, 0) tidal forcing, both the $s^3(3, 3)$ and $s^4(4, 4)$ responses are at the level of $\sim 10^{-6}$ when $\Delta < 10$ per cent and contain significant errors (Figs 2a and b). We believe that a relative amplitude of $\sim 10^{-6}$ for both h_{lm} and k_{lm} is approximately the limit of accuracy that CitcomSVE can reach, given that the numerical models use 12×48^3 elements (or ∼40 km surface resolution) and a 10^{-3} convergence tolerance. However, it is still surprising to see the high accuracy (six orders of magnitude) of CitcomSVE.

Having shown that our perturbation method can determine the spheroidal responses accurately, its accuracy in solving for the toroidal responses is not examined directly. Here we consider the $t^1(2, -1)$ mode and its contributions to $s^2(2, 0)$ and $s^2(2, 2)$ responses for both (2, 0) and (2, 2) tidal forcing. $s^2(2, 0)$ and $s^2(2, 2)$ are also excited from the degree-1 and 3 spheroidal modes (Fig. 1) and this portion of the responses from s to s couplings are believed to be calculated accurately. With the total responses of $s^2(2, 0)$ and $s^2(2, 2)$ being accurate (Table 2), we argue that the $t^1(2, -1)$ solutions should also be accurate. Fig. 3 compares the gravitational responses of both the $s^2(2, 0)$ and $s^2(2, 2)$ modes with (solid lines) and without (dashed lines) the contribution from $t^1(2, -1)$, for $10 \text{ per cent} \leq \Delta \leq 40$ per cent. Without $t^1(2, -1)$, the $s^2(2, 0)$ and $s^2(2, 2)$ responses deviate significantly from the CitcomSVE results. Adding the contribution by $t^1(2, -1)$ eliminates this deviation in the response, which implies that our perturbation method can also determine the toroidal responses accurately.

4.2 (1, 1) lateral heterogeneities in either the bottom or the top half of the mantle

We have shown that our second-order perturbation method accurately solves for the tidal response of a laterally varying Moon with (1, 1) lateral heterogeneities throughout the lunar mantle (case I). To investigate how a Moon with lateral heterogeneities localized to different depth ranges within the mantle would respond to the tidal force, and to test the robustness of our perturbation method, we explore two additional cases that assume the same (1, 1) lateral structure but restrict it to either the bottom (case II) or the top (case III) half of the mantle, respectively.

Downloaded from http://gji.oxfordjournals.org/ at University of Colorado on August 29, 2014

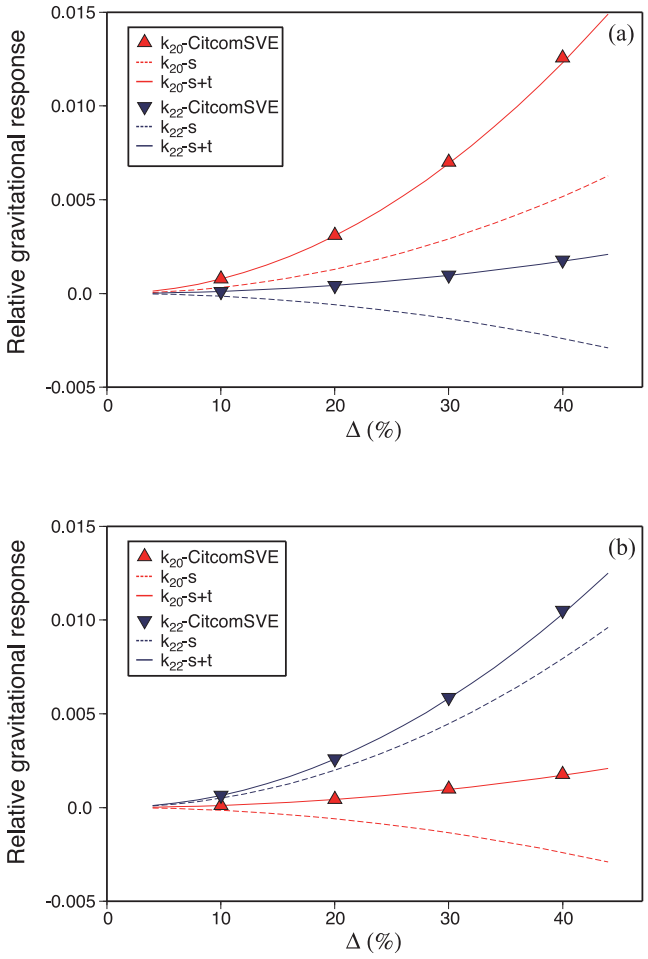

Figure 3. Comparison of the gravitational responses of the self-coupling modes $s^2(2, 0)$ (red) and $s^2(2, 2)$ (blue) with (solid lines) and without (dashed lines) the contribution from $t^1(2, -1)$, for Δ from 10 to 40 per cent. Panels (a) and (b) are for (2, 0) and (2, 2) tidal forcing, respectively. The triangles and inverted triangles are the $s^2(2, 0)$ and $s^2(2, 2)$ responses from the CitcomSVE calculations.

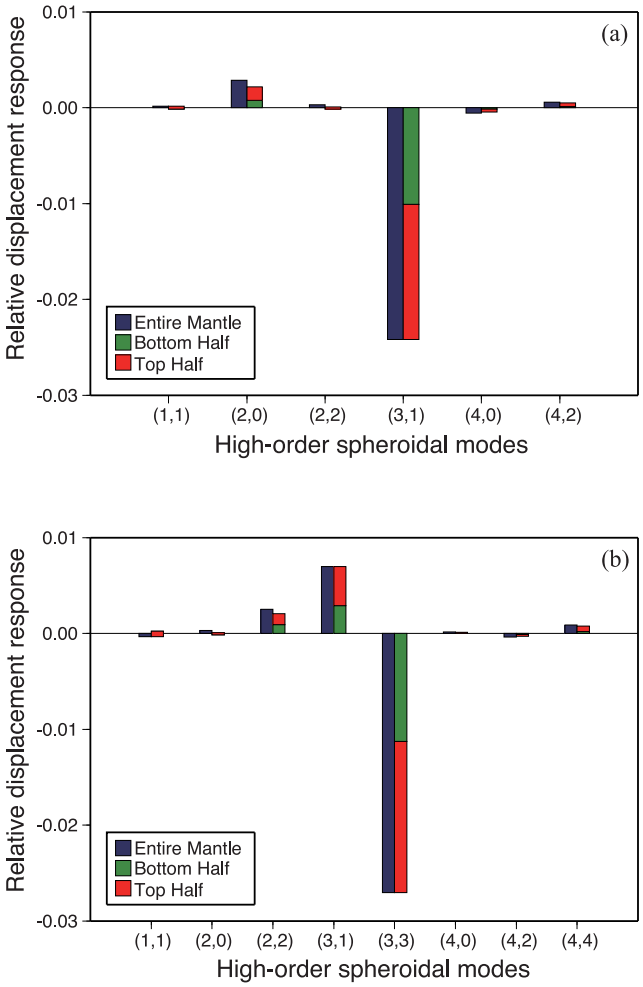

Figure 4. The radial displacement responses of the Moon with (1, 1) shear modulus lateral heterogeneities (I) throughout the entire mantle (blue), (II) in the bottom half of the mantle (green) and (III) in the top half of the mantle (red), for $\Delta = 10$ per cent, to (a) (2, 0) and (b) (2, 2) tidal forcing, respectively. The x-axis lists all the high-order spheroidal response modes. The responses of the same harmonic from cases II and III are summed into one column for comparison with those from case I.

For both cases II and III, the tidal responses to the (2, 0) and (2, 2) tidal forces are calculated for Δ from 2.5 to 40 per cent using both the perturbation method and CitcomSVE. Results for both cases II and III continue to show an overall <1 per cent relative difference in h_{lm} and k_{lm} between these two methods (see Table 2 for $\Delta = 10$ per cent). In Fig. 4, we show the displacement responses, h_{lm}, of each high-order mode for all three cases for both (2, 0) and (2, 2) tidal forcing as $\Delta = 10$ per cent. h_{lm} for cases II and III are added to compare with those in case I. Since case I includes lateral heterogeneities throughout the entire mantle, the high-order responses in case I are generally greater in amplitude than those in cases II and III separately (Fig. 4). However, exceptions exist. The responses $h^1_{1,1}$ for both (2, 0) and (2, 2) tidal forcing in case III are greater than those in cases I and II. However, since cases II and III have non-overlapping depth ranges, and since the sum of their ranges equals the depth range for case I, we expect the sum of the first-order responses from cases II and III to be equal to those from case I, due to linearity of the first-order responses. This is consistent with what we have found in the first-order solutions (Fig. 4). Therefore, it is evident that the responses $h^1_{1,1}$ in cases II and III have opposite signs and thus partially offset one another, explaining the reduced $h^1_{1,1}$ in case I. However, such simple addition cannot be applied to second-order responses (e.g. self-coupling responses), due to non-linear effects (Fig. 4).

4.3 Other long-wavelength structures throughout the mantle

We also use our perturbation method to calculate the tidal response of the Moon for long-wavelength structures other than (1, 1). We consider lateral heterogeneities in the shear modulus throughout the mantle for nine long-wavelength structures, which are harmonics (l_1, m_1) for $1 \leq l_1 \leq 3$ and $0 \leq m_1 \leq l_1$. Here, we use ζ (given in eq. 7), instead of Δ, as our measure of the lateral variability of the shear modulus. Note that we use the total tidal potential that includes both (2, 0) and (2, 2) terms in this scenario.

Fig. 5 shows the high-order gravitational tidal responses of the Moon for all nine laterally heterogeneous structures as $\zeta = 10$ per cent. All the responses are normalized by the primary $s^0(2, 0)$ response. Figs 5(a)–(i) show global maps of the lunar surface gravitational potential anomaly contributed by all the first- and second-order responses, with the sub-Earth point at the centre

Downloaded from http://gji.oxfordjournals.org/ at University of Colorado on August 29, 2014

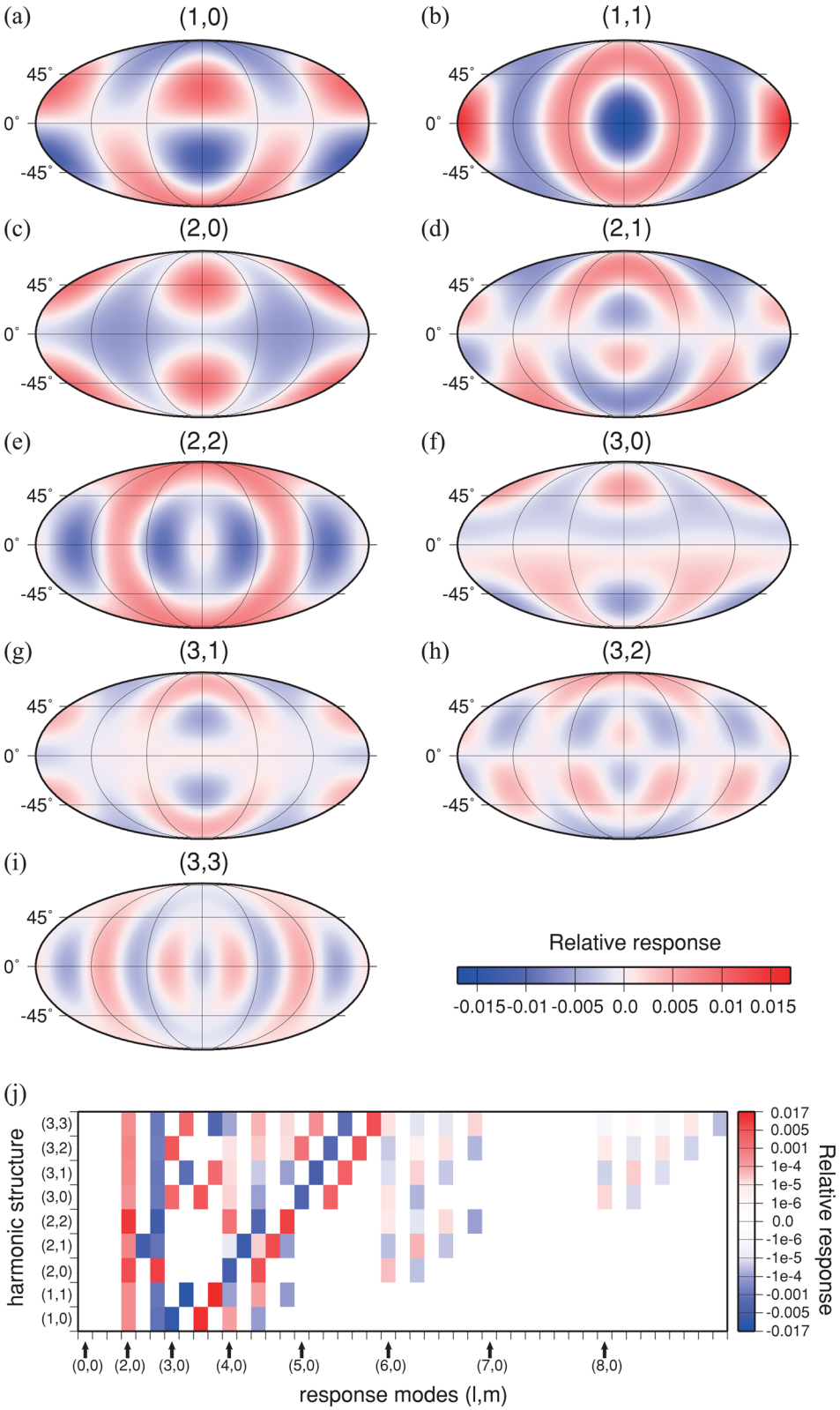

Figure 5. High-order gravitational responses of the Moon to the entire degree-2 tidal force [i.e. the (2, 0) forcing plus the (2, 2) forcing] for each of the long-wavelength laterally heterogeneous structures considered in our paper, with $\zeta_{lm} = 10$ per cent in each case. Panels (a)–(i) are gravitational anomaly maps for the lateral heterogeneities of harmonic (1, 0), (1, 1), (2, 0), (2, 1), (2, 2), (3, 0), (3, 1), (3, 2) and (3, 3), respectively. The centre of the map is the sub-Earth point of the Moon. Panel (j) shows the response spectrum for each harmonic structure. The x-axis represents the high-order spheroidal modes that span from (0, 0), (1, 0), (1, 1), (2, 0), . . . , to (8, 8) in harmonics. The y-axis lists the nine long-wavelength harmonics of the structure. The maps (a)–(i) and the spectral plot (j) use different colour scales.

Downloaded from http://gji.oxfordjournals.org/ at University of Colorado on August 29, 2014

of the map. Fig. 5(j) demonstrates the spectrum of the gravitational responses that spans harmonic degrees 0 to 8 for each associated structure. We make the following observations from our calculations. First, consistent with our selection rules (eq. 22), a degree-1 harmonic structure generates degree-3 first-order and degree-2 and 4 second-order responses; a degree-2 harmonic structure generates degree-2 and 4 first-order and degree-2, 4 and 6 second-order responses; and a degree-3 harmonic structure generates degree-3 and 5 first-order and degree-2, 4, 6 and 8 second-order responses. Secondly, all nine gravitational potential anomaly patterns are dominated mostly by first-order responses with amplitudes ranging from ∼0.2 per cent to less than 2 per cent, relative to the $s^0(2, 0)$ response. Thirdly, the second-order self-coupling modes $s^2(2, 0)$ and $s^2(2, 2)$ show up in all cases, with relative amplitude ranging from 0.04 to 0.07 per cent for $s^2(2, 0)$ and from 0.09 to 0.14 per cent for $s^2(2, 2)$, which are approximately one order of magnitude weaker than most of the first-order modes. However, for some structures, the $s^2(2, 0)$ and $s^2(2, 2)$ responses are comparable with first-order responses that are relatively weak [e.g. $s^1(3, 1)$, 0.2 per cent, in Fig. 5g; $s^1(5, 0)$, 0.14 per cent, in Fig. 5h; $s^1(5, 1)$, 0.04 per cent and $s^1(5, 3)$, 0.19 per cent, in Fig. 5i]. The other second-order responses are two to three orders of magnitude smaller than the first-order responses. Therefore, for lateral variability of 10 per cent or less, we can neglect the second-order non-self-coupling responses. For much larger values of ζ, all the second-order responses become significant and should all be taken into account.

5 CONCLUSION AND DISCUSSION

We have developed a semi-analytic method based on perturbation theory, to solve for the tidal response of a planetary body with 3-D elastic structure in the mantle. The method can be applied to a planetary body where there are weak lateral heterogeneities in the elastic moduli (in this paper, in the shear modulus only) superimposed on a radially stratified reference model. Our second-order perturbation method predicts all the spherical harmonic modes resulting from first- and second-order couplings between the body tide force and the 3-D elastic structure, and determines the responses at these modes. We apply our second-order perturbation method to the Moon to calculate the responses to degree-2 tidal forcing for a variety of laterally heterogeneous lunar mantle structures, including harmonic (1, 1) structure restricted to different depth ranges in the mantle, and other long-wavelength structures with harmonic degrees up to 3.

We also compute the tidal responses for the same models using the 3-D finite element model CitcomSVE. We find remarkable agreement between our perturbation method and the finite element method for small and moderate magnitudes of the perturbation, suggesting that our perturbation method provides accurate solutions to the tidal response problem. Furthermore, our perturbation method provides the first true 3-D benchmark for the finite element code CitcomSVE. The benchmark results show that our finite element model, which has a resolution of ∼40 km at the outer surface with 12×48^3 elements, achieves a relative error of $\sim 10^{-6}$. Since the primary responses (i.e. the tidal love numbers) are generally at the order of 10^{-2}, the high-order responses can be determined accurately down to the level of $\sim 10^{-8}$, which is remarkable. Such a surprisingly small relative error deserves more study from a computational science point of view.

Our perturbation method, which can be used as an alternative to a fully numerical approach, has advantages for solving a tidal response problem. First, our perturbation method is much more time efficient than CitcomSVE in doing forward calculations. For the same problem setup with single harmonic lateral heterogeneity, our perturbation calculation only costs less than 1/10 of the time cost by a CitcomSVE run with 12×48^3 elements. Secondly, our perturbation method is able to directly predict all the spherical harmonic modes in the tidal solution, and the effects of different laterally heterogeneous model parametrizations on each modal coefficient can be investigated individually. This type of mode coupling analysis cannot be easily done using grid-based numerical methods. Thirdly, given observational measurements of the tidal response, inverse modelling to constrain the laterally varying mantle structure would be more efficient using our perturbation method than using a fully numerical approach. Monte Carlo sampling in the parameter space could be easily done to look for plausible long-wavelength pattern(s) and depth range(s) for the mantle lateral heterogeneities that could explain the observations.

A potential application of our perturbation method is to constrain the elastic structure of the present-day lunar mantle, by inverting the gravitational tidal solutions from the GRAIL mission (Zhong *et al.* 2012). Due to the unprecedented accuracy of the GRAIL satellites in measuring the near-surface gravity field, long-wavelength gravitational tidal terms can be determined accurately enough that small tidal variations among different harmonics can be observed and evaluated (Konopliv *et al.* 2013; Lemoine *et al.* 2013). The gravitational tidal signal can be interpreted as a surface representation of the lateral heterogeneities in the lunar interior, and an inversion analysis can thus be performed to determine possible laterally varying structures. It is also important to note out that the degree-2 self-coupling response may cause significant variations in degree-2 Love numbers, thus complicating the usage of degree-2 tidal response to constrain the lunar core size (e.g. Williams 2007).

In the future, our perturbation method can be improved and expanded in the following ways. First, lateral heterogeneities not only in the shear modulus μ (as considered in this paper), but also in the first Lamé parameter λ and density ρ need to be incorporated into our formulation. Secondly, 3-D surface mass loading problems can be solved using our perturbation method by changing only the outer surface boundary condition. Thirdly, our perturbation method can be adapted for tidal or surface loading problems for a planet with an elastic shell of variable thickness (A *et al.* 2014).

ACKNOWLEDGEMENTS

We thank NSF (US-NSF 1114168) and NASA for their financial support. We appreciate Dr Jerry Mitrovica and an anonymous reviewer for their valuable comments and suggestions on our work.

REFERENCES

A, G., Wahr, J. & Zhong, S., 2013. Computations of the viscoelastic response of a 3-D compressible Earth to surface loading: an application to Glacial Isostatic Adjustment in Antarctica and Canada, *Geophys. J. Int.,* **192,** 557–572.

A, G., Wahr, J. & Zhong, S., 2014. The effects of laterally varying icy shell structure on the tidal response of Ganymede and Europa, *J. geophys. Res.,* **119,** 659–678.

Agnew, D.C., 2008. Earth tides, in *Treatise on Geophysics,* Vol. 3: Geodesy, pp. 163–195, eds Herring, T. & Schubert, G., Elsevier.

Dahlen, F.A. & Tromp, J., 1998. *Theoretical Global Seismology,* Princeton Univ. Press, pp. 268–271.

Downloaded from http://gji.oxfordjournals.org/ at University of Colorado on August 29, 2014

Dziewonski, A.M., 1984. Mapping the lower mantle: determination of lateral heterogeneity in *P* velocity up to degree and order 6, *J. geophys. Res.,* **89**(B7), 5929–5952.
Farrell, W.E., 1972. Deformation of the Earth by surface loads, *Rev. Geophys*., **10,** 761–797.
Kaufmann, G. & Wu, P., 2002. Glacial isostatic adjustment on a three-dimensional laterally heterogeneous earth: examples from Fennoscandia and the Barents Sea, in *Ice Sheets, Sea Level and the Dynamic Earth,* Geodyn. Ser., Vol. 29, pp. 293–309, eds Mitrovica, J. X. & Vermeersen, L.L.A., AGU.
Konopliv, A.S. *et al.*, 2013. The JPL lunar gravity field to spherical harmonic degree 660 from the GRAIL Primary Mission, *J. geophys. Res. Planets,* **118,** 1415–1434.
Latychev, K. *et al.*, 2005. Glacial isostatic adjustment on 3-D Earth models: a finite-volume formulation, *Geophys. J. Int*., **161,** 421–444.
Latychev, K. *et al.*, 2009. Body tides on a 3-D elastic Earth: toward a tidal tomography, *Earth planet. Sci. Lett.,* **277,** 86–90.
Lemoine, F.G. *et al.*, 2013. High-degree gravity models from GRAIL primary mission data, *J. geophys. Res. Planets,* **118,** 1676–1698.
Longman, I.M., 1962. A Green's function for determining the deformation of the Earth under surface mass loads: 1. theory, *J. geophys. Res.,* **67,** 845–850.
Longman, I.M., 1963. A Green's function for determining the deformation of the Earth under surface mass loads: 2. computations and numerical results, *J. geophys. Res*., **68,** 485–496.
Nakamura, Y., 2005. Farside deep moonquakes and deep interior of the Moon, *J. geophys. Res.,* **110,** E01001, doi:10.1029/2004JE002332.
Nakamura, Y., Latham, G.V. & Dorman, H.J., 1982. Apollo lunar seismic experiment—final summary, *J. geophys. Res.,* **87**(S01), A117–A123.
Qin, C., Muirhead, A.C. & Zhong, S., 2012. Correlation of deep moonquakes and mare basalts: implications for lunar mantle structure and evolution, *Icarus,* **220,** 100–105.
Richards, M.A. & Hager, B.H., 1989. Effects of lateral viscosity variations on long-wavelength geoid anomalies and topography, *J. geophys. Res.,* **94**(B8), 10 299–10 313.
Tromp, J. & Mitrovica, J.X., 1999. Surface loading of a viscoelastic earth—II. Spherical models, *Geophys. J. Int.,* **137,** 856–872.
Tromp, J. & Mitrovica, J.X., 2000. Surface loading of a viscoelastic planet—III. Aspherical models, *Geophys. J. Int.,* **140,** 425–441.
Van der Hilst, R.D., Widiyantoro, S. & Engdahl, E.R., 1997. Evidence for deep mantle circulation from global tomography, *Nature,* **386,** 578–584.
Wahr, J. *et al.*, 2009. Modeling stresses on satellites due to nonsynchronous rotation and orbital eccentricity using gravitational potential theory, *Icarus,* **200,** 188–206.
Wang, R., 1990. Tidal deformations on a rotating, spherically asymmetric, visco-elastic and laterally heterogeneous Earth, *PhD thesis,* University of Kiel, Kiel, Germany.
Weber, R.C. *et al.*, 2011. Seismic detection of the lunar core, *Science,* **331,** 309–312.
Wieczorek, M.A. *et al.*, 2006. The constitution and structure of the lunar interior, *Rev. Mineral. Geochem.,* **60,** 221–364.
Williams, J.G., 2007. A scheme for lunar inner core detection, *Geophys. Res. Lett.,* **34,** L03202, doi:10.1029/2006GL028185.
Wu, P. & Peltier, W.R., 1982. Viscous gravitational relaxation, *Geophys. J. Int.,* **70,** 435–485.
Zhong, S., Paulson, A. & Wahr, J., 2003. Three-dimensional finite-element modelling of Earth's viscoelastic deformation: effects of lateral variations in lithospheric thickness, *Geophys. J. Int.,* **155,** 679–695.
Zhong, S. *et al.*, 2012. Can tidal tomography be used to unravel the long-wavelength structure of the lunar interior?, *Geophys. Res. Lett.,* **39,** L15201, doi:10.1029/2012GL052362.
Zuber, M.T. *et al.*, 1994. The shape and internal structure of the Moon from the Clementine mission, *Science,* **266,** 1839–1843.
Zuber, M.T. *et al.*, 2013. Gravity field of the Moon from the Gravity Recovery and Interior Laboratory (GRAIL) mission, *Science,* **339,** 668–671.

Downloaded from http://gji.oxfordjournals.org/ at University of Colorado on August 29, 2014

APPENDIX A: VECTOR SPHERICAL HARMONIC EXPANSION OF THE COUPLING TERMS

Any 3-D vector can be expanded in terms of vector spherical harmonics (VSH). In our case, we focus on the VSH expansion of the two vector coupling terms, $\mathcal{F}_D = \nabla \cdot (\delta\mu[\nabla\vec{u}_{D-1} + (\nabla\vec{u}_{D-1})^T])$ in eq. (9) and $\mathcal{B}_D = \hat{r} \cdot [\delta\mu(\nabla\vec{u}_{D-1} + (\nabla\vec{u}_{D-1})^T)]$ in eq. (11), for high-order differential equations (i.e. $D = 1$ or 2). We omit the subscripts D for simplicity.

The real-form spherical harmonic function is defined as

$$Y_{lm} = \begin{cases} \sqrt{2}N_{lm}P_l^m(\cos\theta)\cos m\phi & m > 0 \\ N_{lm}P_l^m(\cos\theta) & m = 0 \\ \sqrt{2}N_{l|m|}P_l^{|m|}(\cos\theta)\sin|m|\phi & m < 0 \end{cases}, \tag{A1}$$

where $P_l^m(\cos\theta)$ is the associated Legendre polynomial of non-negative m, N_{lm} is the normalization constant of non-negative m, and $N_{lm} = \sqrt{\frac{(2l+1)}{4\pi}\frac{(l-m)!}{(l+m)!}}$. The associated derivatives of Y_{lm} are defined as

$$Y_{lm}^{\theta} = \partial_\theta Y_{lm}, \quad Y_{lm}^{\phi} = \frac{1}{\sin\theta}\partial_\phi Y_{lm}, \quad Y_{lm}^{\theta\theta} = \partial_\theta Y_{lm}^{\theta}, \quad Y_{lm}^{\phi\phi} = \frac{1}{\sin\theta}\partial_\phi Y_{lm}^{\phi}, \quad Y_{lm}^{\theta\phi} = \frac{1}{\sin\theta}\partial_\phi Y_{lm}^{\theta}. \tag{A2}$$

The three orthogonal bases of the VSH are defined as (Dahlen & Tromp 1998)

$$\vec{P}_{lm} = \hat{r}Y_{lm}, \quad \vec{B}_{lm} = \nabla_1 Y_{lm}, \quad \vec{C}_{lm} = \hat{r} \times \nabla_1 Y_{lm}, \tag{A3}$$

where $\nabla_1 = \hat{\theta}\frac{\partial}{\partial\theta} + \hat{\phi}\frac{1}{\sin\theta}\frac{\partial}{\partial\phi}$ is the reduced gradient operator. An arbitrary vector $\vec{V}$ can be expanded into VSH as

$$\vec{V}(r,\theta,\phi) = \sum_{l,m}[p_{lm}(r)\vec{P}_{lm} + b_{lm}(r)\vec{B}_{lm} + c_{lm}(r)\vec{C}_{lm}], \tag{A4}$$

where the expansion coefficients p_{lm}, b_{lm} and c_{lm} are functions of r.

We break the two vector coupling terms into spherical components, as

$$\mathcal{F} = C_{1r}\hat{r} + C_{1\theta}\hat{\theta} + C_{1\phi}\hat{\phi},$$
$$\mathcal{B} = C_{2r}\hat{r} + C_{2\theta}\hat{\theta} + C_{2\phi}\hat{\phi}, \tag{A5}$$

where

$$C_{1r} = \partial_r\tau_{rr} + \frac{1}{r}\left(\partial_\theta\tau_{r\theta} + \frac{1}{\sin\theta}\partial_\phi\tau_{r\phi} + 2\tau_{rr} - \tau_{\theta\theta} - \tau_{\phi\phi} + \cot\theta\tau_{r\theta}\right),$$
$$C_{1\theta} = \partial_r\tau_{r\theta} + \frac{1}{r}\left[\partial_\theta\tau_{\theta\theta} + \frac{1}{\sin\theta}\partial_\phi\tau_{\theta\phi} + 3\tau_{r\theta} + \cot\theta(\tau_{\theta\theta} - \tau_{\phi\phi})\right],$$
$$C_{1\phi} = \partial_r\tau_{r\phi} + \frac{1}{r}\left(\partial_\theta\tau_{\theta\phi} + \frac{1}{\sin\theta}\partial_\phi\tau_{\phi\phi} + 3\tau_{r\phi} + 2\cot\theta\tau_{\theta\phi}\right). \tag{A6}$$

Here, the τ'_{ij}s represent the spherical components of the second-order tensor $\vec{\vec{\tau}} = \delta\mu(\nabla\vec{u} + (\nabla\vec{u})^T)$ (note that $\tau_{ij} = \tau_{ji}$), and $\delta\mu$ represents the lateral heterogeneities in the shear modulus μ and is defined by eq. (7) in Section 2.2.

Suppose that $\delta\mu$ has the harmonic pattern (l_1, m_1), and the parent mode is spheroidal, that is $s(l_0, m_0)$. Then, we have

$$\tau_{rr} = 2\zeta\mu_0\dot{U}(r)Y_{l_0m_0}Y_{l_1m_1},$$
$$\tau_{\theta\theta} = \frac{2}{r}\zeta\mu_0\left[U(r)Y_{l_0m_0} + V(r)Y^{\theta\theta}_{l_0m_0}\right]Y_{l_1m_1},$$
$$\tau_{\phi\phi} = \frac{2}{r}\zeta\mu_0\left[U(r)Y_{l_0m_0} + V(r)\left(Y^{\phi\phi}_{l_0m_0} + \cot\theta Y^{\theta}_{l_0m_0}\right)\right]Y_{l_1m_1},$$
$$\tau_{r\theta} = \zeta S(r)Y^{\theta}_{l_0m_0}Y_{l_1m_1},$$
$$\tau_{r\phi} = \zeta S(r)Y^{\phi}_{l_0m_0}Y_{l_1m_1},$$
$$\tau_{\theta\phi} = \frac{2}{r}\zeta\mu_0 V(r)\left(Y^{\theta\phi}_{l_0m_0} - \cot\theta Y^{\phi}_{l_0m_0}\right)Y_{l_1m_1}, \tag{A7}$$

and

$$C_{2r} = 2\zeta\mu_0\dot{U}(r)Y_{l_0m_0}Y_{l_1m_1},$$
$$C_{2\theta} = \zeta S(r)Y^{\theta}_{l_0m_0}Y_{l_1m_1},$$
$$C_{2\phi} = \zeta S(r)Y^{\phi}_{l_0m_0}Y_{l_1m_1}. \tag{A8}$$

For a toroidal parent mode $t(l_0, m_0)$, we have

$$\tau_{rr} = 0,$$
$$\tau_{\theta\theta} = \frac{2}{r}\zeta\mu_0 W(r)\left(\cot\theta Y^{\phi}_{l_0m_0} - Y^{\phi}_{l_0m_0}\right)Y_{l_1m_1},$$
$$\tau_{\phi\phi} = -\tau_{\theta\theta},$$
$$\tau_{r\theta} = -\zeta T(r)Y^{\phi}_{l_0m_0}Y_{l_1m_1},$$
$$\tau_{r\phi} = \zeta T(r)Y^{\theta}_{l_0m_0}Y_{l_1m_1},$$
$$\tau_{\theta\phi} = \frac{1}{r}\zeta\mu_0 W(r)\left(Y^{\theta\theta}_{l_0m_0} - Y^{\phi\phi}_{l_0m_0} - \cot\theta Y^{\theta}_{l_0m_0}\right)Y_{l_1m_1}, \tag{A9}$$

and

$$C_{2r} = 0,$$
$$C_{2\theta} = -\zeta T(r)Y^{\phi}_{l_0m_0}Y_{l_1m_1},$$
$$C_{2\phi} = \zeta T(r)Y^{\theta}_{l_0m_0}Y_{l_1m_1}. \tag{A10}$$

The VSH expansion coefficients of $\mathcal{F}$ and $\mathcal{B}$ at (l, m) are

$$(F^p_{lm}, F^b_{lm}, F^c_{lm}) = \frac{1}{l(l+1)}\iint(\vec{P}_{lm}, \vec{B}_{lm}, \vec{C}_{lm})\cdot\mathcal{F}\,\mathrm{d}\Omega,$$
$$(R^{\mathrm{cp}}_{lm}, S^{\mathrm{cp}}_{lm}, T^{\mathrm{cp}}_{lm}) = \frac{1}{l(l+1)}\iint(\vec{P}_{lm}, \vec{B}_{lm}, \vec{C}_{lm})\cdot\mathcal{B}\,\mathrm{d}\Omega, \tag{A11}$$

Downloaded from http://gji.oxfordjournals.org/ at University of Colorado on August 29, 2014

respectively. In general, a parent mode (s or t) can generate both spheroidal and toroidal child modes. A set of non-zero expansion coefficients at (l, m) from eq. (A11) represents a specific child mode caused by the coupling. Particularly, if a child mode is spheroidal, F^c_{lm} and $T^{\rm cp}_{lm}$ are zero; if a child mode is toroidal, F^p_{lm}, F^b_{lm}, $R^{\rm cp}_{lm}$ and $S^{\rm cp}_{lm}$ are zero.

For each type of parent–child mode pair, the generalized expressions of the non-vanishing r-dependent expansion coefficients are given as follows (the subscript lm is neglected):

(1) $s(l_0, m_0) \otimes (l_1, m_1) \rightarrow s(l, m)$

$$\begin{cases} F^p(r) = c_1\zeta\mu_0\left(\ddot{U} + \dfrac{2\dot{U}}{r} - \dfrac{2U}{r^2} + c_2\dfrac{V}{r^2} + c_3\dfrac{S}{\mu_0 r}\right) \\ F^b(r) = c_4\zeta\mu_0\left(\dfrac{\dot{S}}{\mu_0} + \dfrac{3S}{\mu_0 r} + c_5\dfrac{U}{r^2} + c_6\dfrac{V}{r^2}\right) \end{cases}, \tag{A12}$$

$$\begin{cases} R^{\rm cp}(r) = c_1\zeta\mu_0\dot{U} \\ S^{\rm cp}(r) = c_4\zeta S \end{cases}. \tag{A13}$$

(2) $s(l_0, m_0) \otimes (l_1, m_1) \rightarrow t(l, m)$

$$F^c(r) = c_1\zeta\mu_0\left(\frac{\dot{S}}{\mu_0} + \frac{3S}{\mu_0 r} + c_2\frac{V}{r^2}\right), \tag{A14}$$

$$T^{\rm cp}(r) = c_1\zeta S. \tag{A15}$$

(3) $t(l_0, m_0) \otimes (l_1, m_1) \rightarrow s(l, m)$

$$\begin{cases} F^p(r) = c_1\zeta\left(\dfrac{T}{r}\right) \\ F^b(r) = c_2\zeta\mu_0\left(\dfrac{\dot{T}}{\mu_0} + \dfrac{3T}{\mu_0 r} + c_3\dfrac{W}{r^2}\right) \end{cases}, \tag{A16}$$

$$\begin{cases} R^{\rm cp}(r) = 0 \\ S^{\rm cp}(r) = c_2\zeta T \end{cases}. \tag{A17}$$

(4) $t(l_0, m_0) \otimes (l_1, m_1) \rightarrow t(l, m)$

$$F^c(r) = c_1\zeta\mu_0\left(\frac{\dot{T}}{\mu_0} + \frac{3T}{\mu_0 r} + c_2\frac{W}{r^2}\right), \tag{A18}$$

$$T^{\rm cp}(r) = c_1\zeta T. \tag{A19}$$

Here, $c_1, c_2, \ldots, c_6$ are constant coefficients that measure the strength of the parent–child mode coupling.

For the zeroth-order equations ($D = 0$), $\mathcal{F}_0 = \vec{f}_{\rm td}$. Given the degree-2 tidal force in eq. (6), the VSH expansion of $\mathcal{F}_0$ can be simply obtained using eq. (A11) for (2, 0) or (2, 2) tidal forcing separately, as

$$F^p(r) = -2Z\rho_0 r,\ F^b(r) = -Z\rho_0 r,\ F^c(r) = 0, \tag{A20}$$

where $Z = Z_1$ for (2, 0) tidal forcing while $Z = Z_2$ for (2, 2) tidal forcing, and Z_1 and Z_2 are defined in eq. (5). Since $\mathcal{B}_0$ vanishes,

$$R^{\rm cp}(r) = S^{\rm cp}(r) = T^{\rm cp}(r) \equiv 0. \tag{A21}$$

Apparently from eqs (A20) and (A21), the body tide force, when acting on a spherically symmetric planet, can only induce a spheroidal response.

APPENDIX B: NON–DIMENSIONAL EQUATIONS FOR SPHEROIDAL AND TOROIDAL MODES

We first normalize eq. (21) using the following scalings,

$$r = ar',\quad \rho_0 = \rho_{\rm cmb}\rho_0',\quad \mu_0 = \mu_{\rm cmb}\mu_0',\quad \lambda_0 = \mu_{\rm cmb}\lambda_0',\quad g_0 = 4\pi G\rho_{\rm cmb}ag_0',$$

$$U = aU',\ V = aV',\ W = aW',\ R = \mu_{\rm cmb}R',\ S = \mu_{\rm cmb}S',\ T = \mu_{\rm cmb}T',$$

$$R^{\rm cp} = \mu_{\rm cmb}R^{\rm cp\prime},\ S^{\rm cp} = \mu_{\rm cmb}S^{\rm cp\prime},\ T^{\rm cp} = \mu_{\rm cmb}T^{\rm cp\prime},$$

$$K = 4\pi G\rho_{\rm cmb}a^2K',\ Q = 4\pi G\rho_{\rm cmb}aQ',\ F = \mu_{\rm cmb}/aF', \tag{A22}$$

Downloaded from http://gji.oxfordjournals.org/ at University of Colorado on August 29, 2014

where the primed variables are non-dimensional, a is the Moon's radius, g_0 is the gravitational acceleration, and $\rho_{\rm cmb}$ and $\mu_{\rm cmb}$ are the density and the shear modulus on the mantle side of the CMB. The vector $\boldsymbol{F}$ is determined by the VSH expansion of the mode coupling term, $\mathcal{F}$.

The non-dimensional form of eq. (21) is given by

$$\frac{\mathrm{d}\boldsymbol{X}'}{\mathrm{d}r'} = \boldsymbol{A}' \cdot \boldsymbol{X}' - \boldsymbol{F}'. \tag{A23}$$

Hereafter, all variables are non-dimensional and we omit the primes for simplicity. Note that we do not include the (0, 0) response in our formulation.

1. *Spheroidal mode*

The spheroidal system has six dimensions.

$$\boldsymbol{X} = (U, V, R, S, K, Q)^T, \tag{A24}$$

$$A = \begin{pmatrix} -\frac{2\lambda_0}{r\beta} & \frac{l(l+1)\lambda_0}{r\beta} & \frac{1}{\beta} & 0 & 0 & 0 \\ -\frac{1}{r} & \frac{1}{r} & 0 & \frac{1}{\mu_0} & 0 & 0 \\ \frac{4}{r}\left(\frac{\gamma}{r} - \xi\right) & -\frac{l(l+1)}{r}\left(\frac{2\gamma}{r} - \xi\right) & -\frac{4\mu_0}{r\beta} & \frac{l(l+1)}{r} & -\frac{\xi(l+1)}{g_0 r} & \frac{\xi}{g_0} \\ \frac{1}{r}\left(\xi - \frac{2\gamma}{r}\right) & -\frac{1}{r^2}[2\mu_0 - l(l+1)(\gamma+\mu_0)] & -\frac{\lambda_0}{r\beta} & -\frac{3}{r} & \frac{\xi}{r g_0} & 0 \\ -\rho_0 & 0 & 0 & 0 & -\frac{l+1}{r} & 1 \\ -\rho_0\frac{l+1}{r'} & \rho_0\frac{l(l+1)}{r} & 0 & 0 & 0 & \frac{l-1}{r} \end{pmatrix}, \tag{A25}$$

where $\beta = \lambda_0 + 2\mu_0$, $\gamma = \frac{\mu_0(3\lambda_0+2\mu_0)}{\lambda_0+2\mu_0}$, $\xi = \eta\rho_0 g_0$, l is the harmonic degree, and $\eta = \frac{4\pi G\rho_{\rm cmb}^2 a^2}{\mu_{\rm cmb}}$ is a non-dimensional coefficient. The vector $\boldsymbol{F}$ has the form

$$\boldsymbol{F} = (0, 0, F^p, F^b, 0, 0)^T, \tag{A26}$$

where F^p and F^b are the VSH expansion coefficients defined in eq. (A11). In our calculations, we start the solution process from the CMB and propagate up through the mantle. To find a unique solution to eq. (A23), the boundary conditions at the CMB, the outer surface, and all internal boundaries are needed. The CMB and surface boundary values, $\boldsymbol{X}(r_{\rm c})$ and $\boldsymbol{X}(r_{\rm s})$, are given, respectively by

$$\begin{aligned} \boldsymbol{X}(r_{\rm c}) &= \left[U_{\rm c}, V_{\rm c}, \eta\rho_{0{\rm c}}(K_{\rm c}+g_0 U_{\rm c}), 0, K_{\rm c}, \tfrac{2l+1}{r_{\rm c}}K_{\rm c} + \rho_{0{\rm c}}U_{\rm c}\right]^T, \\ \boldsymbol{X}(r_{\rm s}) &= (U_{\rm s}, V_{\rm s}, 0, 0, K_{\rm s}, 0)^T, \end{aligned} \tag{A27}$$

where $\rho_{0{\rm c}}$ is the density of the fluid core. The last component of both $\boldsymbol{X}(r_{\rm c})$ and $\boldsymbol{X}(r_{\rm s})$ is different from the classical form of the boundary conditions used in tidal forcing problems (Tromp & Mitrovica 2000). The last component in $\boldsymbol{X}(r_{\rm c})$ has been mathematically simplified by assuming a uniform fluid core below the CMB instead of a solid inner core overlain by a fluid outer core. This simplification has little effect on the results. For $\boldsymbol{X}(r_{\rm s})$, which represents the boundary conditions at a free outer surface, the last component is zero instead of the non-zero constant usually used for tidal forcing in the classical form. This classical non-zero constant comes from redefining the gravitational potential variable so that it includes the tidal potential. In that case the effects of the tidal force appear in the outer surface boundary condition instead of in the differential equations. However, in this paper we do not include the tidal potential in the gravitational potential variable, and so the effects of the tidal force appear in the differential equations rather than in the boundary condition.

At any solid–solid internal boundary in the mantle,

$$[U]^+_- = [V]^+_- = [K]^+_- = [Q]^+_- = [R + R^{\rm cp}]^+_- = [S + S^{\rm cp}]^+_- = 0. \tag{A28}$$

Eq. (A28) ensures the continuity of the displacement, the gravitational potential/acceleration, and the radial traction, everywhere in the mantle. Solving for the six unknowns, $U_{\rm c}$,$V_{\rm c}$,$K_{\rm c}$,$U_{\rm s}$,$V_{\rm s}$ and $K_{\rm s}$, uniquely determines the spheroidal response.

2. *Toroidal mode*

For the toroidal mode,

$$\boldsymbol{X} = (W, T)^T, \tag{A29}$$

$$\boldsymbol{A} = \begin{bmatrix} \frac{1}{r} & \frac{1}{\mu_0} \\ \frac{(l+2)(l-1)\mu_0}{r^2} & -\frac{3}{r} \end{bmatrix}, \tag{A30}$$

$$F = (0, F^c)^T, \tag{A31}$$

Downloaded from http://gji.oxfordjournals.org/ at University of Colorado on August 29, 2014

where F^c is defined in eq. (A11). The CMB, outer surface, and internal boundary conditions are given respectively by (Tromp & Mitrovica 2000)

$$\boldsymbol{X}(r_c) = (W_c, 0)^T,$$

$$\boldsymbol{X}(r_s) = (W_s, 0)^T,$$

$$[W]^+_- = [T + T^{cp}]^+_- = 0. \tag{A32}$$

Solving for W_c and W_s determines the toroidal response.

APPENDIX C: PROPAGATOR MATRIX METHOD

Given eq. (21) (or the non-dimensional form eq. A23) and the associated boundary conditions, we apply the fourth-order Runge–Kutta numerical scheme to establish the framework of our propagator matrix method described in Secton 3.3.

In Section 3.3, a 1-D radial grid is set up from the CMB to the outer surface of the mantle. Since continuity conditions must be applied at every internal boundary, we define the grid so that there are two gridpoints at each boundary: one just inside and one just outside. The internal boundaries occur wherever there is a discontinuity, due either to (I) a discontinuity in material properties of the spherical background structure, which causes the matrix $\boldsymbol{A}$ to be discontinuous, or (II) a radial discontinuity in $\delta\mu$. In the latter case, although there is continuity of the radial traction components (see eqs A28 and A32), $\boldsymbol{X}$ and $\boldsymbol{F}$ are discontinuous due to the jump of $\delta\mu$ in the coupling terms. The entire mantle is divided into n layers by all the non-overlapping discontinuity boundaries (Type I plus Type II), and each layer L ($1 \le L \le n$) is equally divided into fine layers with step size h_L. We number all the gridpoints in order from the CMB to the outer surface.

According to the fourth-order Runge–Kutta method, an unknown solution vector$\boldsymbol{X}(r_{i+1})$ can be evaluated from knowledge of $\boldsymbol{X}(r_i)$, as

$$\boldsymbol{X}(r_{i+1}) = \boldsymbol{X}(r_i) + \frac{h_L}{6}(\boldsymbol{K}_1 + 2\boldsymbol{K}_2 + 2\boldsymbol{K}_3 + \boldsymbol{K}_4), \tag{A33}$$

where r_i and r_{i+1} are two neighbouring gridpoints that belong to layer L, and $r_{i+1} = r_i + h_L$. $\boldsymbol{K}_1$, $\boldsymbol{K}_2$, $\boldsymbol{K}_3$ and $\boldsymbol{K}_4$ are defined as

$$\boldsymbol{K}_j = \boldsymbol{M}_j(\boldsymbol{A})\boldsymbol{X}(r_i) + \boldsymbol{N}_j(\boldsymbol{F}), \qquad j = 1, 2, 3, 4, \tag{A34}$$

where $\boldsymbol{M}_j(\boldsymbol{A})$ and $\boldsymbol{N}_j(\boldsymbol{F})$ are given as

$$\begin{aligned}
&\boldsymbol{M}_1(\boldsymbol{A}) = \boldsymbol{A}(r_i),\\
&\boldsymbol{M}_2(\boldsymbol{A}) = \boldsymbol{A}(r_{i+1/2})\left[\boldsymbol{I} + \tfrac{h}{2}\boldsymbol{M}_1(\boldsymbol{A})\right],\\
&\boldsymbol{M}_3(\boldsymbol{A}) = \boldsymbol{A}(r_{i+1/2})\left[\boldsymbol{I} + \tfrac{h}{2}\boldsymbol{M}_2(\boldsymbol{A})\right],\\
&\boldsymbol{M}_4(\boldsymbol{A}) = \boldsymbol{A}(r_{i+1})\left[\boldsymbol{I} + h\boldsymbol{M}_3(\boldsymbol{A})\right],\\
&\boldsymbol{N}_1(\boldsymbol{F}) = \boldsymbol{F}(r_i),\\
&\boldsymbol{N}_2(\boldsymbol{F}) = \boldsymbol{F}(r_{i+1/2}) + \tfrac{h}{2}\boldsymbol{A}(r_{i+1/2})\boldsymbol{N}_1(\boldsymbol{F}),\\
&\boldsymbol{N}_3(\boldsymbol{F}) = \boldsymbol{F}(r_{i+1/2}) + \tfrac{h}{2}\boldsymbol{A}(r_{i+1/2})\boldsymbol{N}_2(\boldsymbol{F}),\\
&\boldsymbol{N}_4(\boldsymbol{F}) = \boldsymbol{F}(r_{i+1}) + h\boldsymbol{A}(r_{i+1})\boldsymbol{N}_3(\boldsymbol{F}),
\end{aligned} \tag{A35}$$

Here, $r_{i+1/2} = (r_i + r_{i+1})/2$, and $\boldsymbol{I}$ is the identity matrix. Eq. (A33) can be rewritten as

$$\boldsymbol{X}(r_{i+1}) = \boldsymbol{P}(r_i, r_{i+1})\boldsymbol{X}(r_i) + \boldsymbol{G}(r_i, r_{i+1}), \tag{A36}$$

where

$$\boldsymbol{P}(r_i, r_{i+1}) = \boldsymbol{I} + \frac{h}{6}[\boldsymbol{M}_1(\boldsymbol{A}) + 2\boldsymbol{M}_2(\boldsymbol{A}) + 2\boldsymbol{M}_3(\boldsymbol{A}) + \boldsymbol{M}_4(\boldsymbol{A})], \tag{A37}$$

and

$$\boldsymbol{G}(r_i, r_{i+1}) = \frac{h}{6}[\boldsymbol{N}_1(\boldsymbol{F}) + 2\boldsymbol{N}_2(\boldsymbol{F}) + 2\boldsymbol{N}_3(\boldsymbol{F}) + \boldsymbol{N}_4(\boldsymbol{F})]. \tag{A38}$$

Eqs (A36)–(A38) are the fundamental equations for our propagator matrix method. $\boldsymbol{P}(r_i, r_{i+1})$ is the differential form of the propagator matrix, and $\boldsymbol{G}(r_i, r_{i+1})$ is the differential contribution of the vector $\boldsymbol{F}$ from r_i to r_{i+1}. Note that when $r_i = r_{i+1}$, $\boldsymbol{P}(r_i, r_{i+1}) = \boldsymbol{I}$ and $\boldsymbol{G}(r_i, r_{i+1}) = 0$.

The differential propagation can be easily generalized to perform the propagation of $\boldsymbol{X}$ from r_i to r_{i+k} ($k > 1$) in the same layer L as

$$\boldsymbol{X}(r_{i+k}) = \boldsymbol{P}(r_i, r_{i+k})\boldsymbol{X}(r_i) + \boldsymbol{G}(r_i, r_{i+k}), \tag{A39}$$

where

$$\boldsymbol{P}(r_i, r_{i+k}) = \boldsymbol{P}(r_{i+k-1}, r_{i+k}) \cdot \boldsymbol{P}(r_{i+k-2}, r_{i+k-1}) \cdot \cdots \cdot \boldsymbol{P}(r_i, r_{i+1}), \tag{A40}$$

and

$$\boldsymbol{G}(r_i, r_{i+k}) = \boldsymbol{G}(r_{i+k-1}, r_{i+k}) + \boldsymbol{P}(r_{i+k-1}, r_{i+k}) \cdot \boldsymbol{G}(r_{i+k-2}, r_{i+k-1}) + \cdots + \boldsymbol{P}(r_{i+1}, r_{i+k}) \cdot \boldsymbol{G}(r_i, r_{i+1}). \tag{A41}$$

Downloaded from http://gji.oxfordjournals.org/ at University of Colorado on August 29, 2014

However, when the propagation reaches a Type II discontinuity boundary at r_b (here, r_b includes the CMB at r_c and the outer surface at r_s), a correction needs to be made to include the discontinuity of $\boldsymbol{X}$. This correction, derived from eqs (A28) and (A32), is

$$\boldsymbol{X}(r_b^+) = \boldsymbol{X}(r_b^-) + \boldsymbol{\varepsilon}\,(r_b)\,, \tag{A42}$$

where $\boldsymbol{\varepsilon}\,(r_b)$ is the correction term that relates the solution vectors $\boldsymbol{X}$ at r_b^- and r_b^+. Specifically, for a spheroidal mode,

$$\boldsymbol{\varepsilon}(r_b) = (0,\, 0,\, R^{cp}(r_b^-) - R^{cp}(r_b^+),\, S^{cp}(r_b^-) - S^{cp}(r_b^+),\, 0,\, 0)^T\,, \tag{A43}$$

while for a toroidal mode

$$\varepsilon(r_b) = [0,\, T^{cp}(r_b^-) - T^{cp}(r_b^+)]^T\,, \tag{A44}$$

where R^{cp}, S^{cp} and T^{cp} are the VSH expansion coefficients defined in eq. (A11). Note that if r_b is equal to r_c (or r_s), R^{cp}, S^{cp} and T^{cp} on the r_c^- (or r_s^+) side are zero since r_c^- (or r_s^+) is out of the solution region. Once across a Type II discontinuity boundary, successive propagation of $\boldsymbol{X}$ continues until reaching another such boundary.

Starting from the CMB boundary value, that is $\boldsymbol{X}(r_c)$, the generalized expression of the solution $\boldsymbol{X}(r_i)$ at any gridpoint can be obtained through

$$\boldsymbol{X}(r_i) = \boldsymbol{P}(r_c, r_i) \cdot \boldsymbol{X}(r_c) + \boldsymbol{G}(r_c, r_i) + E(r_i), \tag{A45}$$

where $\boldsymbol{P}(r_c, r_i)$ and $\boldsymbol{G}(r_c, r_i)$ are the propagator matrix and the propagation of $\boldsymbol{F}$ from r_c to r_i that are defined in eqs (A40) and (A41), respectively. $\boldsymbol{E}(r_i)$ is the total contribution of the correction terms at r_i from all the Type II boundaries below r_i, and

$$\boldsymbol{E}(r_i) = \sum_{r_b \le r_i} \boldsymbol{P}(r_b, r_i) \cdot \boldsymbol{\varepsilon}(r_b) - \delta_{r_i, r_{i+1}} \varepsilon(r_i), \tag{A46}$$

where $\delta_{r_i, r_{i+1}} = 1$ if $r_i = r_{i+1}$ and zero otherwise.

Let r_i in eq. (A45) be r_s, and solve the resulting linear equations eq. (A45), with $\boldsymbol{X}(r_c)$ and $\boldsymbol{X}(r_s)$ given by eq. (A27) for the spheroidal case and eq. (A32) for the toroidal case. After $\boldsymbol{X}(r_c)$ and $\boldsymbol{X}(r_s)$ are fully determined, eq. (21) can be solved at every gridpoint by applying eq. (A45) repetitively.

Downloaded from http://gji.oxfordjournals.org/ at University of Colorado on August 29, 2014